Numerical characterisation and efficient prediction of landslide-tsunami propagation over a wide range of idealised bathymetries

Gioele Ruffini[a,*], Valentin Heller[a], Riccardo Briganti[a]

[a] *Environmental Fluid Mechanics and Geoprocesses Research Group, Faculty of Engineering, University of Nottingham, Nottingham NG7 2RD, U.K.*

Abstract

Landslide-tsunamis are generated by masses, such as landslides or icebergs, impacting into water bodies. Such tsunamis resulted in major catastrophes in the recent past. Generic research into landslide-tsunamis has widely been conducted in idealised water body geometries at uniform water depths. However, varying bathymetries can significantly alter landslide-tsunamis. This article investigates this effect in a 2D flume using selected idealised bathymetries to provide methods to predict the transformed wave characteristics downwave of each feature. The selected bathymetries are: (a) linear beach bathymetries, (b) submerged positive and negative Gaussian bathymetric features and (c) submerged positive and negative step bathymetries. The hydrodynamic model SWASH, based on the non-hydrostatic non-linear shallow water equations, was used to simulate 9 idealised landslide-tsunamis (1 approximate linear, 2 Stokes, 2 cnoidal and 4 solitary waves), for a total of 184 tests. The analysed parameters include the free water surface, wave height and amplitude. Shoaling in (a) is represented by either Green's law or the Boussinesq's adiabatic approximation up to wave breaking with an accuracy of -7% to $+10\%$ for cnoidal and solitary waves, respectively. The results are then analysed with an (i) Artificial Neural Network and (ii) a regression analysis. (i) shows a smaller Mean Square Error (MSE) of 0.0027 than (ii) (MSE = 0.024) and good generalisation in predicting the transformed wave characteristics and, after defining the best dimensionless parameters, (ii) provides empirical equations to predict transformed waves. In addition, simulations were conducted in a 3D basin to investigate the combined effect of the bathymetry and geometry. The efficient use of the developed prediction methods is demonstrated with the 2014 Lake Askja landslide-tsunami where a good accuracy is achieved compared to available numerical simulations.

Keywords: Bathymetry, landslide-tsunamis, long waves, non-linear waves, shoaling, SWASH, wave propagation, wave transformation

*Corresponding author
Email address: gioele.ruffini@outlook.com (Gioele Ruffini)

1. Introduction

1.1. Overview

Tsunamis generated by mass movements (e.g. landslides and icebergs) can be highly destructive events occurring both in enclosed water bodies (Evers et al., 2019b; Gylfadóttir et al., 2017; Harbitz et al., 2014; Panizzo et al., 2005) and the open sea (Chen et al., 2020; Watt et al., 2012; Watts et al., 2005). The term "tsunami" usually applies to impulse waves in the open sea, but it is also used herein to refer to impulse waves in enclosed water bodies. Landslides can be subaerial, i.e. initially located above the Still Water Level (SWL), or submarine, i.e. initially located below the SWL. A catastrophic subaerial landslide-tsunami occurred in the Vajont reservoir in Italy in 1963 where the generated wave overtopped the dam and caused approximately 2000 casualties (Panizzo et al., 2005). Another subaerial landslide-tsunami was generated in 2014 in Lake Askja in Iceland reaching a run up of 80 m (Gylfadóttir et al., 2017). Landslide-tsunamis generated by submarine landslides can be similarly destructive, such as the 10 m high tsunami which impacted Papua New Guinea in 1998 and caused 2100 casualties (Synolakis et al., 2002). These catastrophes can significantly affect people lives and economies of entire countries. Globally, the assessment of potential landslide-tsunamis is relevant especially for "high risk" countries such as China and Norway, where the number of artificial reservoirs and enclosed or constrained water bodies is large. For this reason, reliable hazard assessment techniques are required.

1.2. The effect of the bathymetry on landslide-tsunami propagation

The most reliable approach to perform landslide-tsunami hazard assessments is either a case-specific laboratory or a numerical study that fully considers the details in the water body geometry and bathymetry (Bellotti et al., 2012; Winckler and Liu, 2015). However, studies for the prediction and investigation of landslide-tsunamis for hazard assessment are commonly conducted under more idealised conditions, such as simple water body geometries (2D, laterally constrained waves and 3D, laterally unconstrained waves; Evers et al., 2019a; Heller and Spinneken, 2013, 2015; Huber and Hager, 1997; Jiang and LeBlond, 1994; Kranzer and Keller, 1959; Panizzo et al., 2005; Watts et al., 2005; Wiegel et al., 1970). This further involves a uniform water depth h to investigate effects (e.g. of the water body geometry) without being affected by a varying bathymetry. However, the effect of the bathymetry may become important during tsunami propagation especially close to the shore, i.e. it needs to be taken into account during hazard assessment (e.g. Bellotti et al. 2012; Couston et al. 2015; Romano et al. 2013). A benchmark test case was carried out by Fuchs et al. (2010) analysing landslide-tsunamis propagating over a trapezoidal breakwater in a 2D geometry.

More studies on idealised long waves were mainly conducted of shoaling on beaches or over obstacles. One of these studies is that by Synolakis and Skjelbreia (1993) who analysed the shoaling of solitary waves on a plane beach identifying two shoaling regions and two post breaking regions. The shoaling ones were gradual shoaling, where the wave amplitude a follows Green's law (Green, 1838), and an additional rapid shoaling following the Boussinesq's adiabatic approximation (Synolakis and Skjelbreia, 1993) for beaches with an inclination $\leq 1/50$. The two post breaking regions were modelled with empirical equations. Similar conditions were numerically investigated by Pringle et al. (2016) who estimated h at which shoaling diverges from Green's law. Knowles and Yeh (2018) also investigated shoaling of solitary waves, identifying the ratio L_0/L_f, with L_0 (subscript 0) as the wavelength approaching the beach and L_f as the submerged beach length, as a crucial parameter to determine the shoaling process. More recently, Lalli et al. (2019) presented a generalised formulation of Green's law taking refraction and diffraction on generic bathymetries into account. However, to the authors knowledge, there are no further studies providing universal and easy to apply methods specifically designed to predict landslide-tsunamis downwave of a bathymetric feature.

To address this research gap, the effect of the bathymetry on idealised landslide-tsunamis (non-linear waves representing real landslide-tsunamis) propagation was systematically studied. Herein, the effect of linear beaches and submerged features (i.e. positive and negative Gaussian and step shaped bathymetries) on these idealised landslide-tsunamis is studied, for hazard assessment, mainly using a 2D geometry. These conditions show analogies with gravity wave propagation over submerged natural or artificial features. For this reason, previous studies that investigated non-linear wave propagation over a bar and wave transmission over low crested structures (Beji and Battjes, 1993; d'Angremond et al., 1997; van der Meer et al., 2005; Strusinska-Correia and Oumeraci, 2012, among others) are useful to identify the relevant parameters for the present study. van der Meer et al. (2005) proposed a relationship to predict the transmitted significant wave height by using the incident wave parameters and the submerged feature characteristics. The ratio R_c/H_{m0i}, with H_{m0i} being the incident significant wave height and R_c as the crest freeboard of the structure, was identified as the main parameter. Likewise, wave transformation induced by a sudden change in h, i.e. a step, is a relevant case for the present research; this was numerically investigated by Lara et al. (2011).

The 2D geometry was chosen in the present study to separate the effects of the bathymetry and the water body geometry, apart from Section 6.3 where their combined effect is investigated. The three different bathymetry classes were chosen to reflect a range of conditions in nature. These also involve beach bathymetries, as knowledge of the wave characteristics at the shoreline is useful for the design of structures. The term "transformed" is used in this study to define the wave characteristics resulting from propagation over different bathymetries, e.g. the wave amplitude past a step. As for the incident wave conditions, wave trains are considered (except for solitary waves) as, in general, they represent real tsunamis better than individual waves when using idealised waves and using them avoids spurious numerical contaminations that may occur if a single packet of the same type of waves propagates in still water.

To predict the transformed wave characteristics, the numerical results are analysed by using an Artificial Neural Network (ANN) and regression analysis. The ANN is a sensible choice for this type of investigation due to the complexity of the physical processes involved. An ANN links a specific set of input variables to output ones without assumptions on the relationships among the involved variables showing benefits in identifying correlations that are usually difficult to determine e.g. with a regression analysis. In addition, ANNs were previously successfully used for solving similar coastal engineering problems (Baldock et al., 2019; van Gent et al., 2007; Meng et al., 2020; Panizzo and Briganti, 2007; Panizzo et al., 2005; Pourzangbar et al., 2017, amongst others).

1.3. Aims and Structure

The aim of this study is to efficiently predict wave parameters downwave of bathymetric features or at shorelines for hazard assessments. This is achieved through numerical investigation of the effect of the bathymetry by modelling idealised landslide-tsunamis (approximate linear, Stokes, cnoidal, solitary waves) mostly in a 2D geometry. This leads to the development of an ANN and empirical equations based on regression analysis. In addition, the combined effect of the bathymetry and water body geometry is studied to obtain insight on their non-linear interaction.

The remainder of this article is structured as follows. In Section 2 the methodology with the numerical setup, boundary conditions, calibration and validation processes are explained. The characteristics of the used ANN and the rationale behind the variables included in the regression analysis are also introduced. The water surface time series and the wave heights for each bathymetry are analysed in Section 3. The development of the ANN and the results of the regression analysis are shown in Sections 4 and 5, respectively. In Section 6, the combined effect of the bathymetry and geometry is analysed and discussed for a 3D geometry. In addition, the results of both predictive approaches are analysed and applied to the 2014 Lake Askja case. Finally, Section 7 highlights the main conclusions and future work.

2. Methodology

The numerical investigation in this study was conducted with the non-hydrostatic Non-Linear Shallow Water Equations (NLSWEs) numerical model SWASH (Stelling and Duinmeijer, 2003; Zijlema and Stelling, 2005; Zijlema et al., 2011). SWASH is well suited for this study as it can accurately simulate fundamental phenomena such as frequency dispersion (using multiple layers), diffraction, shoaling and breaking for landslide-tsunami propagation over the three different selected bathymetry classes (Section 2.1). A Simple architecture for the ANN was defined (Section 2.2) and, using knowledge of the physical processes involved, the non-dimensional parameters for the regression analysis were defined (Section 2.3).

2.1. Numerical setup

SWASH v4.01 was used to model the propagation of idealised landslide-tsunamis in mainly 2D geometries with regular grids. SWASH solves the depth averaged non-hydrostatic NLSWEs which were expanded in Stelling and Zijlema (2003) to the multi-layer case used herein.

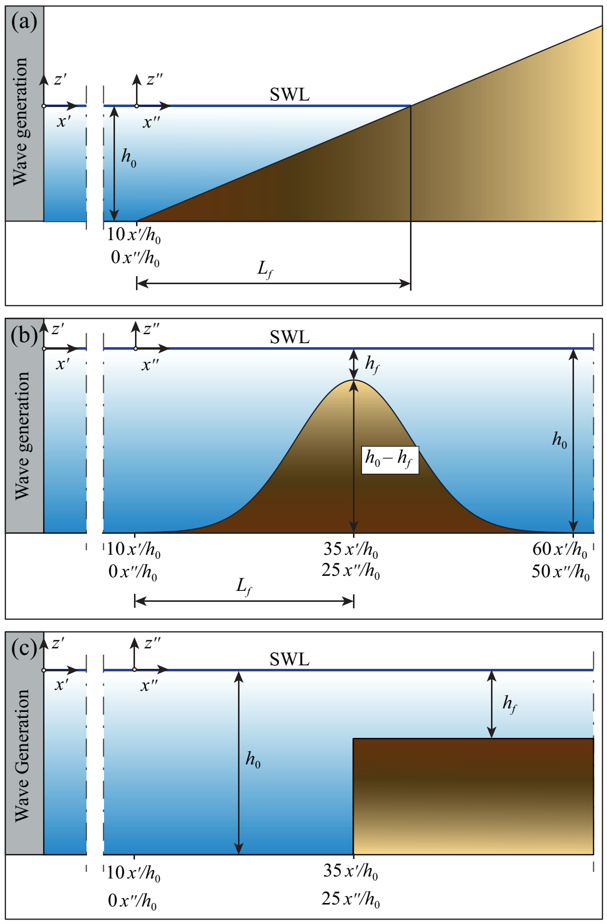

Figure 1: Schematic representations of the three investigated bathymetries with the most relevant parameters: (a) linear beach, (b) Gaussian bathymetric features and (c) step bathymetries.

2D geometries were investigated using numerical flumes with a uniform width of 0.6 m in the y' direction. Three different classes of bathymetries were investigated, namely (a) linear beach bathymetries (Fig. 1a), (b) positive and negative Gaussian bathymetric features (Fig. 1b) and (c) positive and negative step bathymetries (Fig. 1c). Bathymetries (a) and (c) were chosen to assess the impact of landslide-tsunamis on the opposite coast in a basin. The main reason for investigating (b) was to expand the set of conditions with an underwater feature (e.g. a shoal, submerged island or structure) that can alter the tsunami offshore before reaching the coast. For each wave condition a simulation with $h =$ constant was carried out as reference for the results. A coordinate system with $x' = 0$ at the interface between the generation and propagation zones is used, as in Ruffini et al. (2019). Two different coordinate systems were defined in the flume length direction, x' with the origin at the wave generation boundary and x'' with the origin at $x' = 10h_0$ with h_0 as the initial water depth, where the water depth changed for (a) and (b). The use of a uniform h region after wave generation ensured that the waves were stable at the start of the bathymetric feature. Wave gauges were placed at intervals of $\Delta x'' = h_0$ starting from $x''/h_0 = 0$.

The beach inclinations $1/20, 1/30, 1/50$ and $1/70$ were defined by the ratio h_0/L_f as shown in Fig. 1a, with L_f being the submerged length of the feature. Gaussian shapes are given by

$$z''(x'') = [(h_0 - h_f)e^{-(x''-c_1)^2/(2c_2^2)}] - h_0 \tag{1}$$

where h_f is the water depth at the crest/trough of the feature, c_1 is the position of the centre of the Gaussian bathymetric feature at $x'' = 25h_0$ and $c_2 = 6.67h_0$ specifies its width. Note that for this bathymetry, L_f is defined as the first half of the feature. 10 different cases classified by h_f (Table 1) were chosen, 5 positive and 5 negative cases. The same ten values were also used for the step where the instantaneous change in water depth occurs at $25x''/h_0$ (Table 1). Note that the step occurs between two adjacent grid points.

Table 1: Ratios between the water depth h_f at the crest/trough and the initial water depth h_0 for both the Gaussian and step tests.

	Positive cases	Negative cases
$\frac{h_f}{h_0}$	0.1	1.3
	0.2	1.6
	0.3	1.7
	0.4	1.8
	0.7	1.9

The numerical model was compiled with the Intel compiler 2017 and Intel-MPI libraries for the use with multiple processors using the Message Passing Interface (MPI) protocol. A stripwise decomposition method along the $y'-$axis was chosen. All simulations were carried out using the High Performance Computing (HPC) cluster of the University of Nottingham.

2.1.1. Boundary conditions

All numerical tests were carried out with a wave source width of $b' = 0.60$ m and the incident water surface elevation η_i of the wave conditions as input for which the fundamental parameters are summarised in Table 2. H_i is the incident wave height, T the incident wave period (note that there is no subscript since its value does not change during propagation), L_i the incident wavelength, a_i the incident wave amplitude and c_i the wave celerity. Note that, in the following, the definition $H = a + a_{th}$ applies, where a_{th} is the wave trough, reducing for linear waves to $H = 2a$.

Different slide scenarios lead to different wave types usually associated with theoretical non-linear waves (e.g. Heller and Hager, 2011; Panizzo et al., 2005). For this reason, all η_i time series for the investigated idealised landslide-tsunamis, are calculated using 5$^{\text{th}}$ order Stokes (Fenton, 1985), 5$^{\text{th}}$ order cnoidal (Fenton, 1999) and 1$^{\text{st}}$ order solitary (Boussinesq, 1872) wave theories. Approximate linear waves are used for grid calibration, consistently with Ruffini et al. (2019), and to expand the range of wave conditions. This wave type can also be associated to very dispersive landslide-tsunamis which, with increasing propagation distance, will approximate $H/a \approx 1$, similarly as linear waves (Evers et al., 2019b; Heller and Hager, 2011; Heller and Spinneken, 2015; Panizzo et al., 2005). In Table 2, the approximate linear waves and non-linear wave conditions specified with "I" are the same as in Ruffini et al. (2019). Conditions referred as "II" are additional wave conditions, one for each of the non-linear Stokes, cnoidal and solitary wave types. Two more wave conditions, namely "III" and "IV", were added for the Gaussian and step bathymetries with $h_f/h_0 = 0.1$ to 0.4 to expand the dataset for the ANN. The wave parameters for every wave condition in Table 2 are based on Heller and Hager (2011). Each incident wave condition was investigated in every bathymetry described in Section 2.1, apart from "III" and "IV", resulting in 184 tests in total.

Table 2: Wave conditions used in this study with the wave parameters based on Heller and Hager (2011). The wave conditions marked with * are only used in a subset of the tested bathymetries.

Wave condition	h_0 (m)	H_i (m)	T (s)	L_i (m)	a_i (m)	c_i (m/s)
Approximate linear	0.600	0.040	0.876	1.190	-	-
Stokes I	0.600	0.100	1.000	1.530	-	-
Cnoidal I	0.300	0.155	1.740	2.830	0.110	1.630
Solitary I	0.300	0.159	-	-	0.159	1.969
Stokes II	0.600	0.240	1.910	4.120	-	-
Cnoidal II	0.300	0.208	1.430	2.740	0.164	1.910
Solitary II	0.300	0.173	-	-	0.173	1.903
Solitary III*	0.300	0.164	-	-	0.164	1.850
Solitary IV*	0.300	0.175	-	-	0.175	1.740

The wave generation boundary was defined as a segment at $x' = 0$ m using a weakly reflective boundary condition (Blayo and Debreu, 2005). This assumes a wave direction perpendicular to the boundary with an incident depth averaged velocity $\bar{u}_i$ defined by

$$\bar{u}_i = \pm\sqrt{\frac{g}{d}}(2\eta_i - \eta) \tag{2}$$

including the total water depth d, gravitational acceleration g and the total (incident + reflected) water surface elevation η. In addition, all lateral walls were represented by closed boundaries with zero flux velocity (Stelling and Zijlema, 2003). For simulations involving wave trains, only steady wave heights after the initial warming up of the model were considered and a ramping up function was added to smooth the wave initiation in each simulation. To avoid wave reflection from the downwave end of the domain, a sponge layer (Dingemans, 1997), with a length of at least $3L_i$, was used for the Gaussian and step bathymetry cases. For solitary waves the sponge layer was 15 m long. Wave breaking was considered in all simulations. In SWASH this was achieved by switching to the hydrostatic computation, therefore using the intrinsic dissipation mechanism of the NLSWEs for breaking waves (Zijlema et al., 2011), in the presence of steep bore-like waves. These waves were tracked when the vertical speed of the free water surface $\partial\eta/\partial x'$ exceeded the default of $0.6\sqrt{gh}$, where 0.6 represents the maximum local surface steepness. The calculation at that specific point switched back to non-hydrostatic only if $\partial\eta/\partial t' < 0$. A second, lower, threshold for $\partial\eta/\partial x'$ was used at $0.3\sqrt{gh}$ to label neighbouring points to simulate the persistence of wave breaking (i.e. presence of wave breaking in more than a single point at a given time).

Finally, the formulation based on Manning's roughness coefficient n was chosen for the bottom friction coefficient c_f as

$$c_f = \frac{n^2 g}{d^{1/3}} \tag{3}$$

In the present study, $n = 0.009$ s/m$^{1/3}$ for glass was chosen for all geometries to mimic the 2D experimental conditions of Heller and Hager (2011).

2.1.2. Calibration and numerical schemes

All cases were simulated using a Cartesian grid with $\Delta x' = \Delta y' = 2.5$ cm, consistently with Ruffini et al. (2019), for which the results satisfied the symmetry and convergence of the solution. SWASH uses higher order dispersion relations with the order matching the number of layers over the water depth. Higher values of kh, with k being the wave number, require more layers. 2 layers were chosen in the present work; tests carried out in SWASH (2016) show a maximum error between the numerical and the shallow water wave celerities of 1% for $kh \leq 7.7$.

Approximate linear and Stokes I waves were simulated using a higher order upwind discretisation scheme for the vertical advection term of the $\overline{u}$-momentum equation, where $\overline{u}$ is the depth averaged velocity in the x'-direction, while the default 1$^{\text{st}}$ order upwind scheme was used for the remaining waves. This was necessary to reduce numerical dissipation, observed in the approximate linear and Stokes I wave propagation, using the 1$^{\text{st}}$ order scheme (SWASH, 2016). For these wave types the central differencing scheme was also used for the vertical advection term of the $\overline{w}$-momentum equation, where $\overline{w}$ is the depth averaged velocity in the z'-direction (SWASH, 2016). In addition, for the step bathymetry for approximate linear and Stokes I waves, the central differencing scheme for the horizontal advection term of the $\overline{u}$-momentum equation, was replaced with the backward differencing scheme to eliminate instabilities caused by the default one. Finally, for the step bathymetries with $h_f/h_0 = 1.7$, 1.8 and 1.9 for approximate linear waves and $h_f/h_0 = 1.8$ and 1.9 for Stokes waves I and II, the bottom step had to be smoothed over 3-4 neighbour grid points to avoid model crashing. Only 4.0% of the simulations were smoothed, thus the impact on the overall results is very limited.

Finally, the time integration, relying on the Courant-Friedrichs-Lewy condition and wave celerity, for the present study is defined as

$$C_r = \Delta t' \left(\sqrt{gd} + \sqrt{\overline{u}^2 + \overline{v}^2} \right) \sqrt{\frac{1}{\Delta x'^2} + \frac{1}{\Delta y'^2}} \leq 1 \tag{4}$$

where C_r is the Courant number, $\Delta t'$ the time step, $\overline{v}$ the depth-averaged velocity in the $y'-$direction and $\Delta x'$ and $\Delta y'$ are the distances between two grid points in the direction of the wave propagation x' and the perpendicular direction y'. To calculate the time step, minimum and maximum C_r thresholds were applied in order to accurately control the convergence of the solution.

2.2. Artificial Neural Network

ANNs are structured in layers, as shown in Fig. 2, with different functions. The input layer is composed of m variables. For this study, these variables include 4 different input parameters taken from simulations with $h =$ constant at $x''/h_0 = 0$, namely H_0/h_0, a_0/h_0, L_0/h_0 and $T(g/h_0)^{1/2}$, as well as the reciprocal of the bathymetry inclination $L_f/(h_0 - h_f)$ and the ratio between the water depth over the feature and the initial water depth h_f/h_0 representing the role of the bathymetry. The last two parameters were chosen to easily identify and approximate the main characteristics of every bathymetry. The output variables are the transformation coefficient $K_b = H_b/H_0$, i.e. the ratio of the transformed wave height H_b after each bathymetry (subscript b) feature with H_0, and the amplitude transformation coefficient $K_{a,b} = a_b/a_0$, i.e. the ratio between the transformed wave amplitude a_b and a_0, respectively. Therefore, 6 input and 2 output parameters were used.

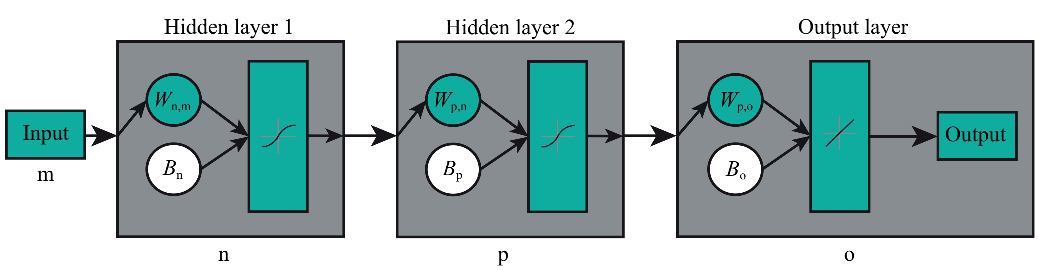

Figure 2: ANN scheme in which m represents the number of inputs, n and p the number of neurons and o the number of outputs.

Fig. 2 shows the notation used to indicate each layer and its number of elements. The subscript m is the number of elements in the input layer, o the number of outputs and n and p are the number of neurons in the first and second hidden layers, respectively. The input and target were first scaled between 1 and -1 as

$$Y_{\mathrm{j}} = 2\frac{(X_{\mathrm{j}} - X_{min,\mathrm{j}})}{(X_{max,\mathrm{j}} - X_{min,\mathrm{j}})} + 1 \quad (5)$$

where Y_{j} and X_{j} are the scaled and unscaled arrays of the parameters, respectively, with j = m for the input and j = o for the outputs. $X_{max,\mathrm{j}}$ and $X_{min,\mathrm{j}}$ are the arrays of the maximum and minimum values of every variable in X_{j}, respectively. The hidden layers have the purpose of defining the connections between the inputs and targets and are composed of a predefined number of neurons. Here, two hidden layers were used, with the same number p = n of neurons, which provided the best performance. Each neuron in each layer has an initial and final activation value that determine the strength of the connections between elements of different layers. For the first hidden layer the initial activation values form the array $A1'_{\mathrm{n}}$, defined by the weighted sum:

$$A1'_{\mathrm{n}} = W_{\mathrm{n,m}} Y_{\mathrm{m}} + B_{\mathrm{n}} \quad (6)$$

where $W_{\mathrm{n,m}}$ is the weights matrix of n by m elements, and B_{n} is the bias array that identifies a constant for each neuron. The values of $W_{\mathrm{n,m}}$ and B_{n} are defined during the training of the ANN as explained in the next paragraph. The array of the final activation values for the first hidden layer $A1_{\mathrm{n}}$ is determined using a Sigmoid symmetric transfer function:

$$A1_{\mathrm{n}} = 2/(1 + e^{-2A1'_{\mathrm{n}}}) - 1 \quad (7)$$

returning an array with n elements. $A1_{\mathrm{n}}$ is used as the input for the second layer, for which the initial and final arrays of the activation values $A2'_{\mathrm{p}}$ and $A2_{\mathrm{p}}$, respectively, were calculated following the same procedure, i.e. solving Eqs. (6) and (7) but using the weight matrix $W_{\mathrm{p,n}}$ and bias array B_{p}, specific for the second layer, resulting in an array with p elements.

Subsequently, the activation values array of the output layer was found as

$$A3'_{\mathrm{o}} = W_{\mathrm{o,p}} A2_{\mathrm{p}} + B_{\mathrm{o}} \quad (8)$$

where $W_{\mathrm{o,p}}$ is the weight matrix of o by p elements and a bias array B_{o} specific for this layer (recall that o is the number of outputs of the ANN). The linear transfer function $A3_{\mathrm{o}} = A3'_{\mathrm{o}}$ was used to determine the scaled output values predicted by the ANN. Finally, the normalisation based on Eq. (5) at the start of the calculation is reversed to determine the actual unscaled values of the output predicted by the ANN.

The development of an ANN generally follows three steps: training, validation and testing. The dataset was randomly divided with 80% employed for training, 10% for validation and the remaining 10% for testing. Training is an iterative process consisting of learning epochs (i.e training steps) that are used to increase the performance of the ANN in predicting the target values starting from the inputs. The development of the ANN was conducted with MATLAB®

in this study. The Levenberg-Marquardt optimisation algorithm (Hagan and Menhaj, 1994; Marquardt, 1963), the default algorithm in MATLAB®, was used to minimise the performance parameter, which was the Mean Square Error (MSE) between target (known) and predicted values. The validation, occurring simultaneously to the training, was used to stop the former if the performance for this part of the dataset failed to improve for a specific number of epochs. The final weight matrices $W_{\mathrm{n,m}}$, $W_{\mathrm{p,n}}$ and $W_{\mathrm{o,p}}$ and arrays B_{n}, B_{p} and B_{o} were defined at the end of these two steps. Finally, the testing is used to assess the generalisation of the ANN, e.g to find out if it applies to datasets other than those used for training, by comparing the MSE obtained for the two steps. The ANN was considered accurate and reliable when the MSE was at least of the order of 10^{-2} and close between the ones of the training and testing steps. This value was deemed acceptable in Panizzo and Briganti (2007) for a similar range of predictions.

2.3. Choice of parameters for regression analysis

Three non-dimensional parameters were used as independent variables to carry out the regression analysis. These parameters were chosen because they are readily available during hazard assessment of landslide-tsunamis, also this study builds upon the choice of parameters carried out in studies on wave transmission (Beji and Battjes, 1993; d'Angremond et al., 1997; van der Meer et al., 2005). All these studies identify as leading non-dimensional parameters the ones that best represents the wave energy transformation induced by the feature. Following this consideration, the first parameter chosen was h_f/h_0 as it identifies the amount of energy transformed downwave of each bathymetric feature by only considering the difference in h. Alternatively, the parameter $(h_f/h_0)(a_0/H_0)$ was defined, i.e. a combination of $h_f//h_0$ and a_0/H_0, being indicative of the wave type allowing both the characterisation of the bathymetry and incident waves in a single parameter. The last parameter is h_f/H_0 in a stricter analogy with R_c/H_{m0} as the main parameter in the prediction of wave transmission (e.g van der Meer et al., 2005) (Section 1.2).

3. Results

3.1. Water surface time series

The time series for the first four wave types shown in Table 2 are hereafter discussed for the steepest slope or smallest h_f for every bathymetry class illustrating the most extreme cases. Five consecutive T, after a steady H was reached in the simulations, are shown. For this representation the time t' is taken as zero at the start of the first shown T. Fig. 3a shows η over the normalised time t'/T for the 1/20 beach at $x''/h_0 = 0$ (black solid line) compared with the one from Ruffini et al. (2019), where a flat bottom was used (red solid line), to show the effect of reflection. Reflection from the beach has a small effect on η in this case. The transformed η (dashed black line) measured at the shoreline suggests that approximate linear waves result in the largest loss of wave energy during breaking for this bathymetry class. Here, H at the shoreline is 3.2 times smaller than at $x''/h_0 = 0$. Fig. 3b shows the results for the Gaussian bathymetric feature for $h_f/h_0 = 0.1$ and η over the feature ($x''/h_0 = 25$, solid gray line) is also included. Given that the water depth returns to h_0 after the hump, the energy dissipated due to breaking is much smaller than in Fig. 3a. The transformed wave at $x''/h_0 = 50$ recovers to an approximate linear wave but with a 1.5 times smaller H than at $x''/h_0 = 0$. Fig. 3c shows the results for the step case with $h_f/h_0 = 0.1$ where η at $x''/h_0 = 0$ is the bathymetry in which reflection is the strongest. Due to reflection upwave of the step, a is +58.6% of that of a flat bottom which is the reason behind the larger vertical axis in Fig. 3. The transformed waves in this case were investigated at $x''/h_0 = 31$ instead of 25 to allow the waves to adapt to h_f.

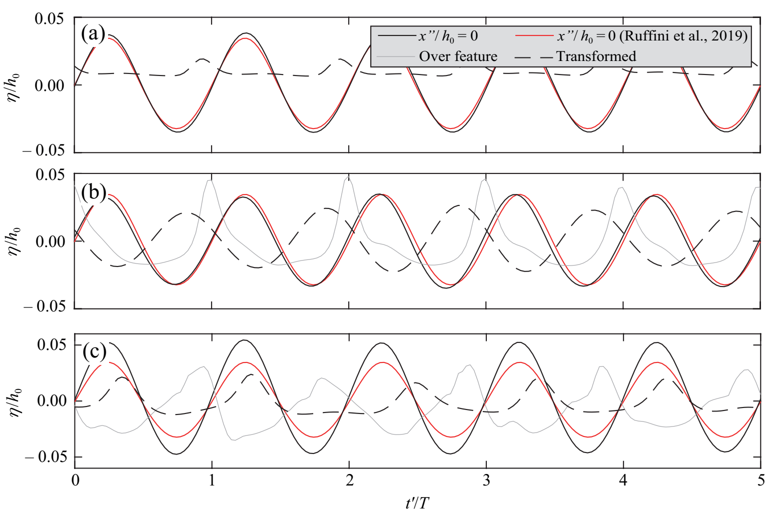

Figure 3: Normalised water surface elevation η/h_0 versus time normalised with the wave period t'/T for approximate linear waves for the (a) 1/20 beach (transformed η at $x''/h_0 = 30$, i.e. at the shoreline), (b) Gaussian bathymetric feature with $h_f/h_0 = 0.1$ (transformed η at $x''/h_0 = 50$) and (c) step with $h_f/h_0 = 0.1$ (transformed η at $x''/h_0 = 41$).

Fig. 4 includes the results for Stokes I waves for the same bathymetries as in Fig. 3. Reflection becomes more significant than in Fig. 3 with η for the Gaussian bathymetric feature in Fig. 4b also being characterised by a phase lag at $x''/h_0 = 0$ compared to the results for a horizontal bottom. The beach bathymetry once again results in the largest wave dissipation, compared to the remaining bathymetry classes, with H at the shoreline 6.9 times smaller than at $x''/h_0 = 0$. Note that this behaviour is also due to the conditions under which each time series was recorded, especially for the beach where $h_f = 0$. In that case the waves can not stabilise again since onshore of that position the idealised landslide-tsunami starts to run-up on the initially dry beach.

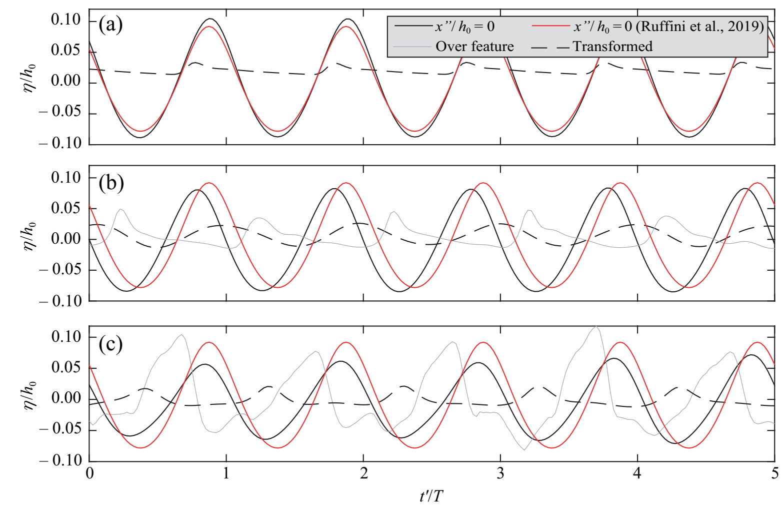

Figure 4: Normalised water surface elevation η/h_0 versus time normalised with the wave period t'/T for Stokes I waves for the (a) 1/20 beach (transformed η at $x''/h_0 = 30$, i.e. at the shoreline), (b) Gaussian bathymetric feature with $h_f/h_0 = 0.1$ (transformed η at $x''/h_0 = 50$) and (c) step with $h_f/h_0 = 0.1$ (transformed η at $x''/h_0 = 41$).

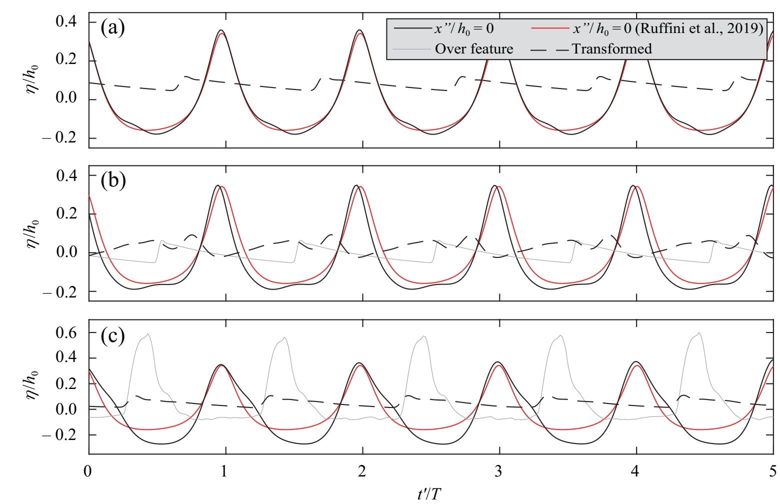

Figure 5: Normalised water surface elevation η/h_0 versus time normalised with the wave period t'/T for cnoidal I waves for the (a) 1/20 beach (transformed η at $x''/h_0 = 30$, i.e. at the shoreline), (b) Gaussian bathymetric feature with $h_f/h_0 = 0.1$ (transformed η at $x''/h_0 = 50$) and (c) step with $h_f/h_0 = 0.1$ (transformed η at $x''/h_0 = 41$).

Fig. 5 shows the results for cnoidal I waves. In two of the three cases the waves break and propagate as bores at the point where the transformed waves are investigated. Note that for Fig. 5c the vertical axis has increased limits due to the larger η values caused by the sudden decrease in water depth of the step bathymetry. In this case, reflection is more significant at $x''/h_0 = 0$ where the wave trough a_{th} is 1.7 times larger than for the flat bathymetry, however, a is virtually unaffected.

Solitary I waves are shown in Fig. 6 where the time is normalised as $t'(g/h_0)^{1/2}$, showing the same general behaviours as for the previous wave types. However, solitary waves dissipate much less energy E (where $E = H^2\rho_w g/8$, with ρ_w being the water density) due to breaking. E at the shoreline becomes 1/4 of the incident one due to the transformed H being 1/2 of H_0 (Fig. 6a). Fig. 6c reveals that a more than doubles at the step ($x''/h_0 = 25$) before breaking. The impact on the step also generates the largest reflected wave reaching $x''/h_0 = 0$ with cnoidal wave characteristics ($a/a_{th} = 7.5$) at $t'(g/h_0)^{1/2} = 75$.

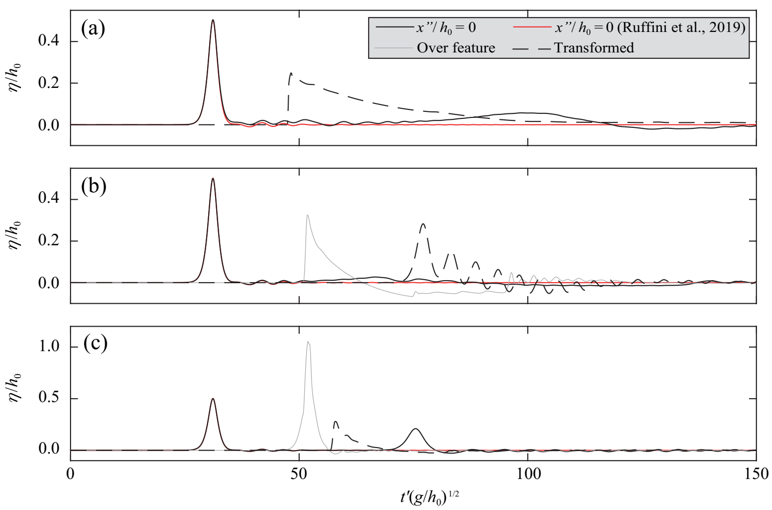

Figure 6: Normalised water surface elevation η/h_0 versus time normalised as $t'(g/h_0)^{1/2}$ for solitary I waves for the (a) 1/20 beach (transformed η at $x''/h_0 = 30$, i.e. at the shoreline), (b) Gaussian bathymetric feature with $h_f/h_0 = 0.1$ (transformed η at $x''/h_0 = 50$) and (c) step with $h_f/h_0 = 0.1$ (transformed η at $x''/h_0 = 41$).

3.2. Wave heights distribution

For the analysis of the distribution along the flume, H and a were calculated as the average over $10T$ (except for the solitary wave). Note that on the beaches $H = a$ was considered downwave of the shoreline, where H was calculated as $\eta_{max} - z''_{bed}$ where η_{max} is the maximum of η for each T and z''_{bed} is the bed level at each position. Only the value at the initial shoreline position was then used in the prediction methods, therefore excluding run-up.

The H values along the beach were calculated at discrete intervals of $\Delta x'' = h_0$ starting from $x''/h_0 = 0$. Fig. 7 shows the relative wave height H/h_0 for the beach bathymetries for all "I" wave conditions. By using the normalised vertical bathymetry coordinate $z''(x'')/h_0$ on the horizontal axis H/h_0 collapses on the vertical axis for nearly all investigated wave types. The vertical dashed line at $z''(x'')/h_0 = 0$ represents the shoreline position with negative values pointing offshore. Hence, positive values represent wet points on the initially dry beach.

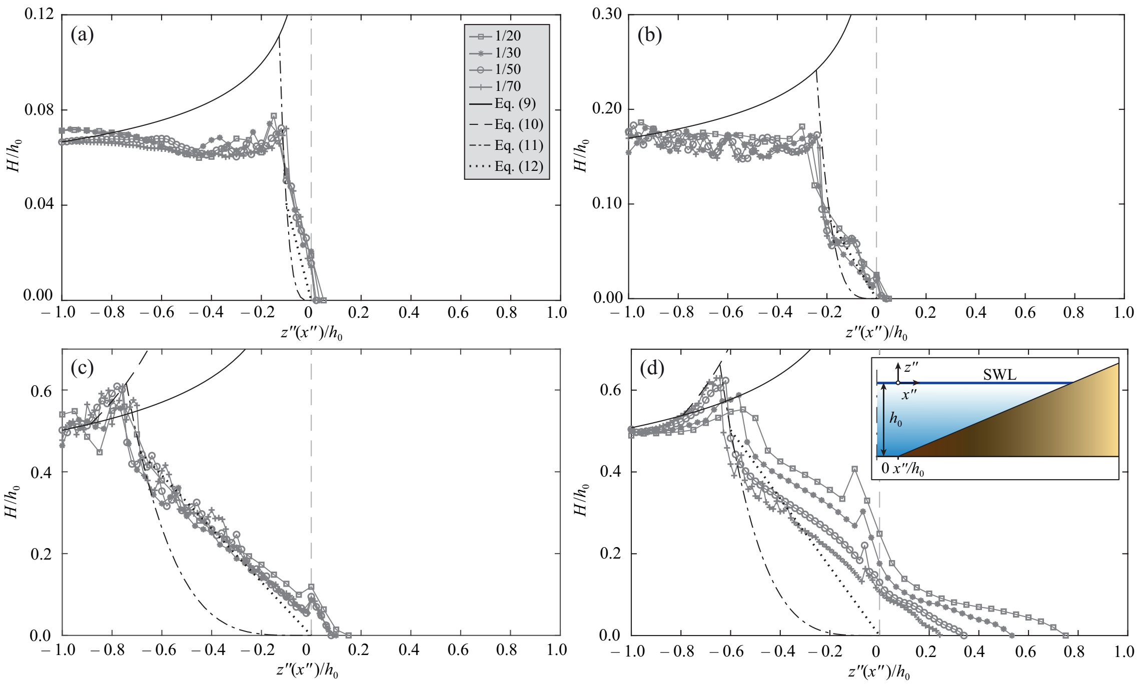

Figure 7: Linear beach bathymetries: relative wave height H/h_0 versus the normalised vertical bathymetry coordinate $z''(x'')/h_0$ for (a) approximate linear waves, (b) Stokes I waves, (c) cnoidal I waves and (d) solitary I waves compared to Green's law (Eq. (9)), Boussinesq's results (Eq. (10)) and decay laws after breaking (Eqs. (11) and (12)). (— —) represents the position of the shoreline.

To validate the results, each panel in Fig. 7 also includes Green's law given by

$$H = H_0(h_0/h)^{1/4} \tag{9}$$

and Boussinesq's results derived from the adiabatic solution

$$H = H_0(h_0/h), \tag{10}$$

representing the gradual and rapid shoaling zones (Synolakis and Skjelbreia, 1993). Further, the two laws of Synolakis and Skjelbreia (1993) that model the decay due to breaking are

$$H = H_0(h_0/h)^{-4}, \tag{11}$$

and

$$H = H_0(h_0/h)^{-1}. \tag{12}$$

Eq. (11) models the initial rapid decay stage, while Eq. (12) represents the successive gradual one. H/h_0 for approximate linear and Stokes I waves (Fig. 7a,b), respectively, do not follow Green's law closely until breaking (at $z''(x'')/h_0 = -0.12$ for approximate linear and $z''(x'')/h_0 = -0.24$ for Stokes I waves). The relative differences between the maximum predicted and modelled H and a before breaking are calculated as $\Delta f(H \text{ or } a) = (f_{pred}/f_{num} - 1) \times 100$ with f_{pred} as the predicted value by Eq. (9) or Eq. (10) (to calculate the amplitude, a and a_0 are used instead of H and H_0 in both equations) and f_{num} as the numerical results. These ratios are presented in Table 3. Values of up to $\Delta f(H) = +64\%$ were found by using Eq. (9) for approximate linear and $\Delta f(H) = +42\%$ for Stokes I waves. However, using a instead of H, Eq. (9) provided better results (Fig. A.1a,b) with $\Delta f(a) = +14\%$ for these two wave types (Table 3). After breaking, the two distinct decay zones from Synolakis and Skjelbreia (1993) describe the behaviour of H especially for the Stokes I waves (Fig. 7b), where a distinct change in decay from Eq. (11) to Eq. (12) can be noticed at $z''(x'')/h_0 = -0.20$.

In Fig. 7c, H/h_0 for cnoidal I waves first follows Eq. (9) and subsequently, at $z''(x'')/h_0 = -0.86$, starts to follow Eq. (10) such that both shoaling zones are present for this wave type. Due to this, H_0 in Eq. (10) is replaced with the predicted H by Eq. (9). Eq. (10) is then applied from the position where the modelled H starts to diverge until breaking occurs. This applies to every investigated slope except for 1/20 where the rapid shoaling zone is absent.

Table 3: Relative differences between the predictions based on Eqs. (9) and (10) and the numerical results in Figs. 7 and A.1 for the maximum values of H and a before breaking. * marks cases where Eqs. (9) and (10) are applied in succession, whereas all the remaining cases are predicted by only using Eq. (9). To predict a, H is replaced with a and a_0 with H_0 in Eqs. (9) and (10).

		Beach inclination			
		1/20	1/30	1/50	1/70
Approximate linear	H	+38%	+40%	+57%	+64%
	a	+10%	+14%	+14%	+13%
Stokes I	H	+26%	+37%	+40%	+42%
	a	+9%	+9%	+13%	+11%
Cnoidal I	H	−4%	+0.3%*	−0.5%*	−0.4%*
	a	−4%	−7%*	−7%*	−6%*
Solitary I	H	+7%	−0.4%	+10%*	+6%*
	a	+6%	−0.01%	+7%*	+4%*

For solitary I waves (Fig. 7d) and slopes $\geq 1/30$, H only follows Eq. (9) whereas, for slopes $\leq 1/50$, it follows Eq. (9) and successively Eq. (10) from $z''(x'')/h_0 = -0.80$. This is in line with Synolakis and Skjelbreia (1993) where both shoaling regions were only found for slopes $\leq$1/50. However, the decay after breaking is not well captured by Eqs. (11) and (12) where a smaller decay for the solitary I waves is found. The agreement with Eqs. (9) and (10) is always better for more non-linear waves where Δf up to +0.3% for cnoidal I waves and −0.4% for solitary I waves for the maximum H are found before breaking (Table 3).

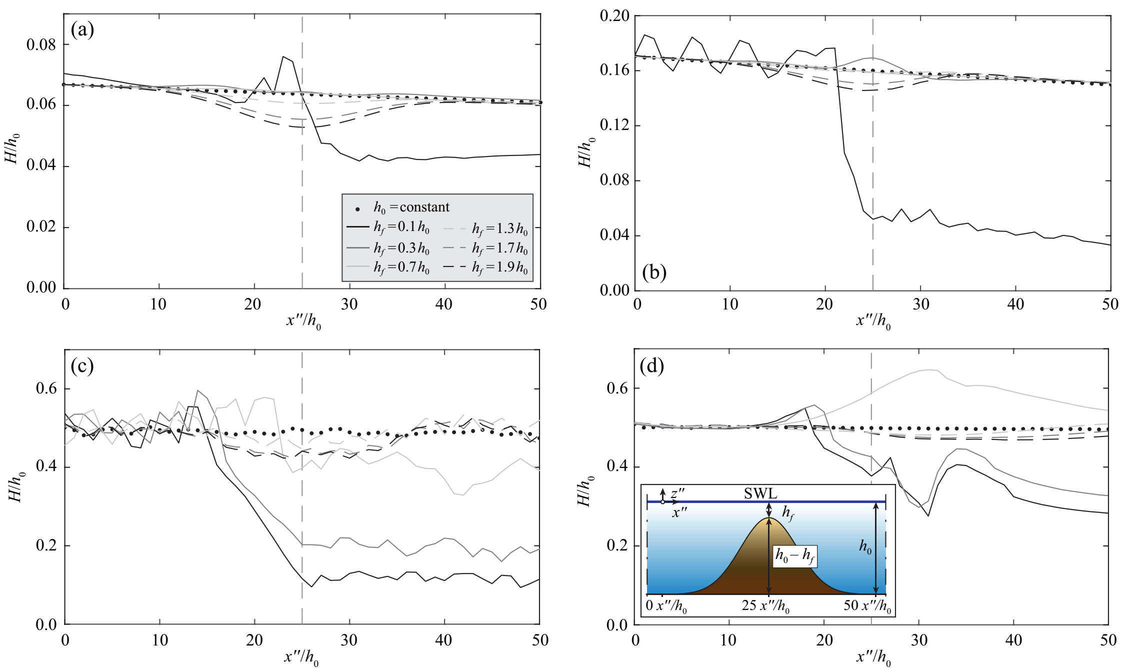

Figure 8: Positive and negative Gaussian bathymetric features: relative wave height H/h_0 versus the relative distance x''/h_0 for (a) approximate linear waves, (b) Stokes I waves, (c) cnoidal I waves and (d) solitary I waves. (— —) highlights x''/h_0 of the maximum or minimum of the bathymetries.

Fig. 8 shows H/h_0 over the normalised propagation distance x''/h_0 for each Gaussian bathymetric features for the approximate linear, Stokes I, cnoidal I and solitary I waves. For negative bathymetries (dashed lines) the waves are affected locally only at the deepest points and the transformed H coincide with that on a flat horizontal bottom. Differences are only found for the solitary I wave (Fig. 8d) because H/h_0 recovers more slowly than for other wave types, resulting in a slightly lower transformed H/h_0 than for h_0 = constant. The positive Gaussian bathymetric features (solid lines) result in two distinct spatial distributions regardless of the wave type: if breaking occurs, it is always upwave of h_f with a sharp loss of H/h_0 afterwards; if breaking does not occur, the transformed H/h_0 at $x''/h_0 = 50$ recovers to the same value as for h_0 = constant. The only exception is, again, the solitary I wave (Fig. 8d) for $h_f/h_0 = 0.7$ where the tsunami propagates over the bathymetry and the transformed H/h_0 increases by a factor of 1.06 compared to the one at $x''/h_0 = 0$. Note that for this specific case, the maximum H/h_0 is found at $x''/h_0 = 41$, after the position of h_f, showing that shoaling affects H/h_0 without causing breaking. H/h_0 only starts to adjust again to the increasing h after that position.

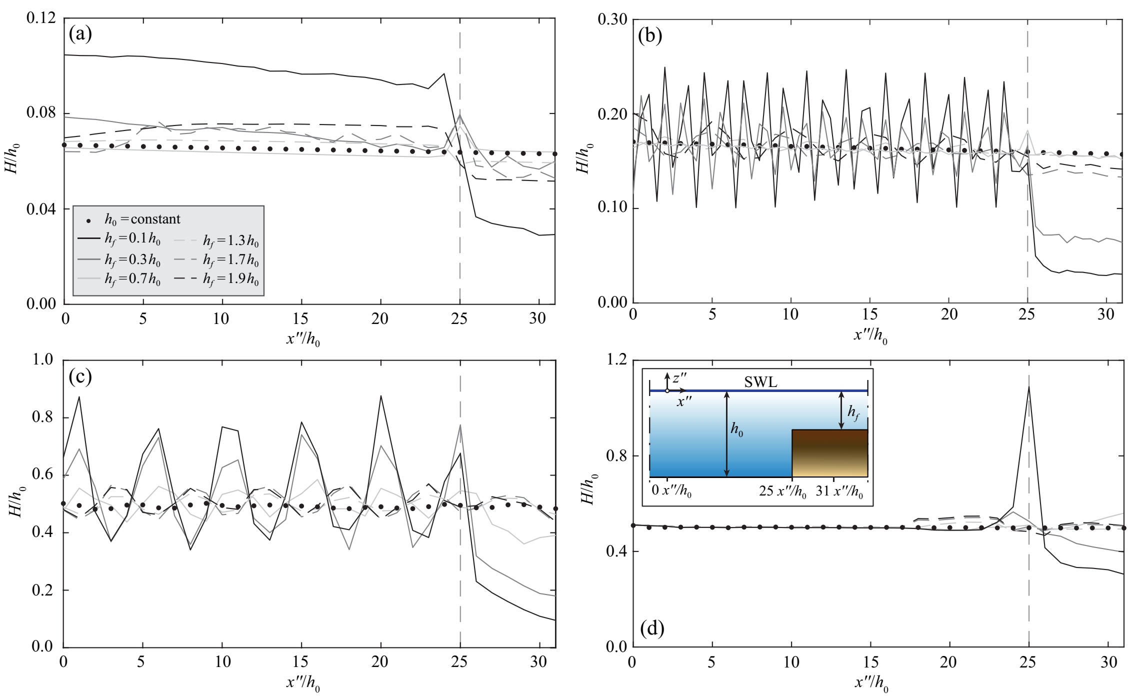

Figure 9: Positive and negative step bathymetries: relative wave height H/h_0 versus the relative distance x''/h_0 for (a) approximate linear waves, (b) Stokes I waves, (c) cnoidal I waves and (d) solitary I waves. (— —) highlights x''/h_0 of the positive or negative step.

The results for H/h_0 for the steps are shown in Fig. 9. They confirm that the reflection is stronger (Section 3.1) for all cases with $h_f<h_0$, compared to the results for other bathymetry classes. This is particularly noticeable for approximate linear waves (Fig. 9a) for which, for the step with $h_f/h_0 = 0.1$, H/h_0 are 1.8 times larger than the values for a flat bathymetry at $x''/h_0 = 0$. The transformed H/h_0 at $x''/h_0 = 31$ increases as the step lowers reaching the value for a flat bottom when $h_f/h_0 = 0.7$ for approximate linear and Stokes I waves (Fig. 9a,b). In Fig. 9b,c modulations of H/h_0 occur. This phenomenon is due to wave reflection from the step generating a partially standing wave with a modulation of $L_i/2$ for Stokes I waves and cnoidal I waves. Note that for Stokes I waves in this specific case, the number of wave gauges to calculate H was doubled to avoid aliasing of the wavelength of the standing wave present up to $x''/h_0 = 25$.

In the bathymetries where $h_f>h_0$, the step affects the transformed H/h_0 much less with values very close or slightly smaller than for a horizontal bottom. The only exceptions are the approximate linear waves, for which the values are comparable to some of the ones with $h_f<h_0$. In addition, a small high frequency reflection is noticed for all wave types upwave of the step which are likely limitations of the numerical model in dealing with sudden changes in h. The corresponding figures to Figs. 7 to 9 for a are presented in Appendix A.

4. Data analysis with an Artificial Neural Network

The ANN was used to analyse the data of all simulations employing 6 input parameters, i.e. H_0/h_0, a_0/h_0, L_0/h_0, $T(g/h_0)^{1/2}$, $L_f/(h_0-h_f)$ and h_f/h_0, to predict the 2 output parameters K_b and $K_{a,b}$ (Section 2.2). The initial calibration and optimisation of the ANN architecture together with the final ANN error distribution are illustrated hereafter.

4.1. Calibration and optimisation of the ANN

The ANN was first calibrated to determine a suitable number of neurons for the present dataset. The Mean Square Error MSE and the Pearson correlation coefficient $\rho(\text{pred},\text{target})$ were calculated for each ANN step. The MSE is defined as

$$\text{MSE} = \frac{1}{\text{N}}\sum_{\text{j}}^{\text{N}}\left(f_{\text{pred,j}} - f_{\text{target,j}}\right)^2 \tag{13}$$

and $\rho(\text{pred},\text{target})$ as

$$\rho(\text{pred},\text{target}) = \frac{Cov(\text{pred},\text{target})}{Std(\text{pred})Std(\text{target})}. \tag{14}$$

In Eq. (13) $f_{\text{pred,j}}$ is the j-th sample of the predicted ANN output and $f_{\text{target,j}}$ is the corresponding ANN target and N is the number of samples in each separate step (i.e. training, validation and testing). In Eq. (14) Cov(pred, target) is the covariance between output and target and Std(pred) and Std(target) are the standard deviations. $\rho(\text{pred},\text{target})$ is used as complementary performance parameter to better measure the correlation between outputs and targets with 1 representing complete correlation and 0 no correlation.

Calibration and optimisation were performed by evaluating the best balance between increasing number of neurons and increasing performance, i.e lower MSE and higher $\rho(\text{pred},\text{target})$. However, in the present application, increasing the number of neurons in each layer, at some point, results in negligible effects on the ANN performance, at the same time increasing the computational complexity results in bigger weight matrices and bias arrays.

The data used in the training, validation and testing steps were randomly selected. Therefore, for a representative performance value for the ANN when testing different numbers of neurons, the median values of MSE and $\rho(\text{pred},\text{target})$ were calculated after repeating randomisation and all ANN steps 30 times.

The ANN was tested with 5, 10, 15, 20, 25 and 30 neurons for each of the 2 hidden layers to compare the results and to identify the best number of neurons.

The performance is shown in Fig. 10 with the training and test steps compared including the median values for each number of neurons represented by the solid lines. Fig. 10a shows that the MSE steadily decreases but reveals very similar values for ≥ 15. The $\rho(\text{pred}, \text{target})$ (Fig. 10b) show the same behaviour with an inverse trend. For this reason, a final architecture using 2 hidden layers with 15 neurons each was chosen as it also showed the best performance between the training and test steps. This is a good indicator of the capabilities of the ANN to predict a different dataset accurately. The values of the performance parameters for both training and testing of the final chosen ANN are presented in Table 4.

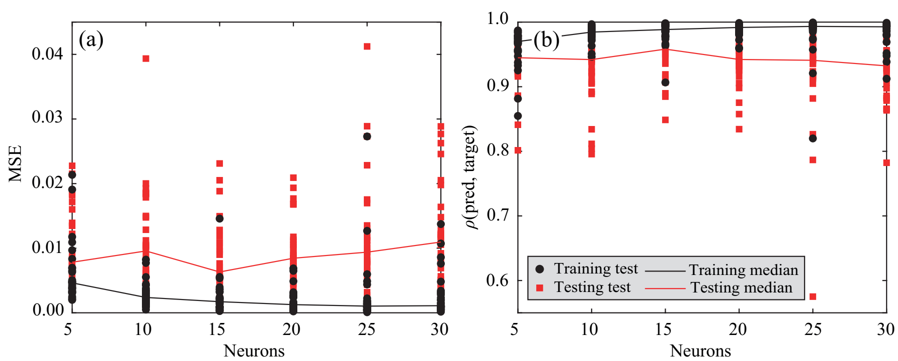

Figure 10: ANN performance comparison for different numbers of neurons for the training and testing steps (a) MSE and (b) Pearson coefficient $\rho(\text{pred}, \text{target})$.

Table 4: Comparison between training and testing MSE and $\rho(\text{pred}, \text{target})$ for the chosen ANN.

	MSE	$\rho(\text{pred}, \text{target})$
Training	0.0011	0.99
Testing	0.0027	0.98

4.2. ANN error distribution

The regression plot based on the chosen ANN is shown in Fig. 11a with the comparison between the target values (horizontal axis) and the output predictions (vertical axis) for the complete dataset with K_b and $K_{a,b}$ combined. The dashed lines are the 95% confidence intervals to determine the spread of the predictions from the perfect agreement (solid line) confirming the good performance of the ANN with intercepts at ± 0.076. Fig. 11b shows the error columns chart with the classes of errors between targets and outputs on the horizontal axis and the number of instances for each class on the vertical axis. In addition, the normal distribution of the error was tested and verified for two different variations of Kolmogorov-Smirnov tests (Öner and Deveci Kocakoç, 2017). Appendix B includes more details on the ANN including $W_{\text{n,m}}$, $W_{\text{p,n}}$, $W_{\text{o,p}}$, B_{n}, B_{p} and B_{o}.

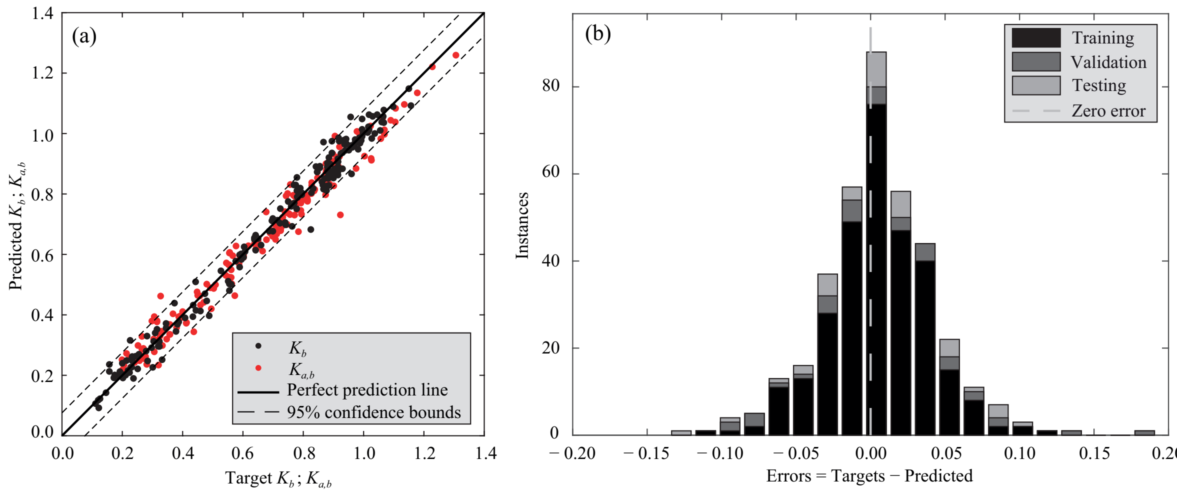

Figure 11: ANN results: (a) regression plot with perfect prediction line and 95% confidence bounds and (b) error columns chart for all three steps involved in the ANN generation.

5. Regression Analysis

Regression analysis of the numerical results of all 184 simulations was also used to obtain empirical equations for the investigated idealised landslide-tsunamis. The variability of K_b and $K_{a,b}$ was tested against different input parameters to find a simple correlation to forecast the idealised landslide-tsunamis downwave of different bathymetries. The three different non-dimensional parameters h_f/h_0, $(h_f/h_0)(a_0/H_0)$ and h_f/H_0 (Section 2.3), were chosen to describe K_b and $K_{a,b}$. The values from test 3 of Fuchs et al. (2010) were also included to compare the predictions of the newly derived equations with laboratory measurements.

Fig. 12a shows the relation between K_b and the ratio h_f/h_0. The best fit to the data was achieved with the following curve (black line):

$$K_b = 0.23 + 0.77\left(\frac{2(h_f/h_0)}{1+(h_f/h_0)^2}\right); \quad \text{MSE} = 0.021. \tag{15}$$

$K_b = 0.23$ in Eq. (15) ensures that the curve intersects the median of the data at $h_f/h_0 = 0$ and the pre-term $(1 - 0.23) = 0.77$ assures that the curve reaches the physically meaningful value $K_b = 1$ at $h_f/h_0 = 1$ (corresponding to $h =$ constant). 75% of the data lies within the ±30% bounds which is a surprisingly small scatter, considering the wide range of bathymetries represented simply by h_f/h_0. When approaching $h_f/h_0 = 1$, $K_b > 1$ in some cases. This is due to H being enhanced by the bathymetry through shoaling and reflection and either not breaking or not fully recovering to its original value downwave of the feature.

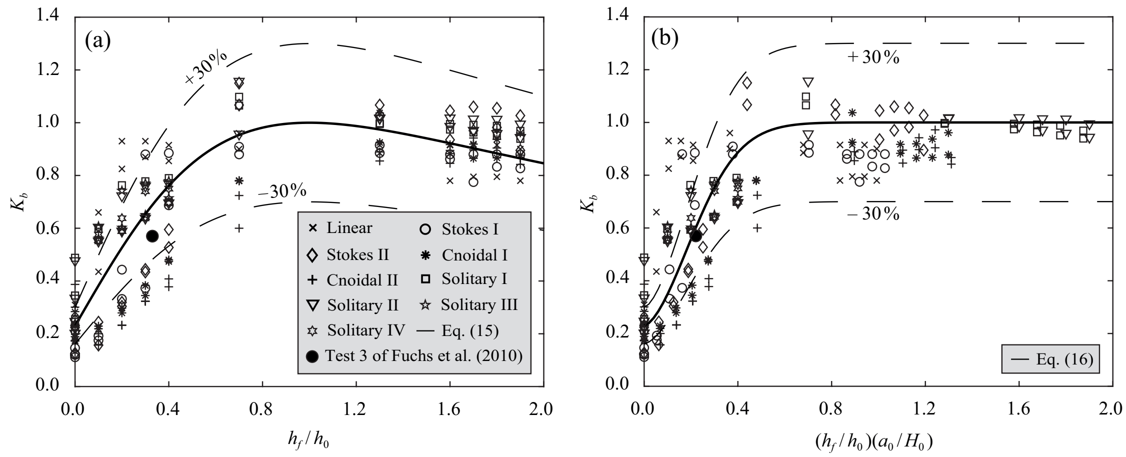

Figure 12: Transformation coefficient K_b for all wave types and bathymetries versus (a) h_f/h_0 with (——) Eq. (15) and (b) $(h_f/h_0)(a_0/H_0)$ with (——) Eq. (16); (— —) represent the ±30% bounds.

The parameter $(h_f/h_0)(a_0/H_0)$ is presented on the horizontal axis of Fig. 12b allowing to better consider the initial wave conditions (Section 2.3). For example, solitary waves ($a_0/H_0 = 1$) only depend on h_f/h_0, hence they remain at the same positions in Fig. 12a and b. The best fit of the data in Fig. 12b was achieved with a hyperbolic tangent (tanh) as

$$K_b = 0.23 + 0.77 \tanh^{[1-(h_f/h_0)(a_0/H_0)]}(4[(h_f/h_0)(a_0/H_0)]^{3/2}); \quad \text{MSE} = 0.024. \tag{16}$$

Eq. (16) represents the data for $(h_f/h_0)(a_0/H_0) \geq 1.4$ with the maximum deviation equal to +6.5% between the predicted and numerical values. The data for both Stokes and cnoidal waves for $(h_f/h_0)(a_0/H_0) \leq 0.4$ are better represented by Eq. (16) (Fig. 12b) than by Eq. (15) (Fig. 12a). However, a small number of points are shifted slightly further away from the prediction curve such as for the approximate linear waves when $(h_f/h_0)(a_0/H_0) \leq 0.44$. Eq. (16) is designed to reach $K_b = 1$ when $(h_f/h_0)(a_0/H_0) = 0.75$, which is the average value between linear ($a_0/H_0 = 0.5$) and solitary ($a_0/H_0 = 1$) waves for h = constant. Eq. (16) also better agrees with the experimental value from Fuchs et al. (2010).

The variability of K_b against h_f/H_0 is shown in Fig. 13 with a zoom provided in Fig. 13b. Here the prediction law is presented similarly to Eq. (15) as

$$K_b = 0.23 + 0.77 \left(\frac{1.29(h_f/H_0)}{0.59 + (h_f/H_0)^{1.1}} \right)^2; \quad \text{MSE} = 0.024. \tag{17}$$

The equation was designed to reach $K_b = 1$ at $h_f/H_0 = 5$ and to decrease afterwards due to bottom friction. Eq. (17) closely follows the data of K_b in

Fig. 13a for $h_f/H_0 \geq 5$ and Fig. 13b shows that it better represents the results for $h_f/H_0 \geq 1$ than for $h_f/H_0 < 1$. Overall, Eq. (17) results in a slightly less good fit than Eqs. (15) and (16).

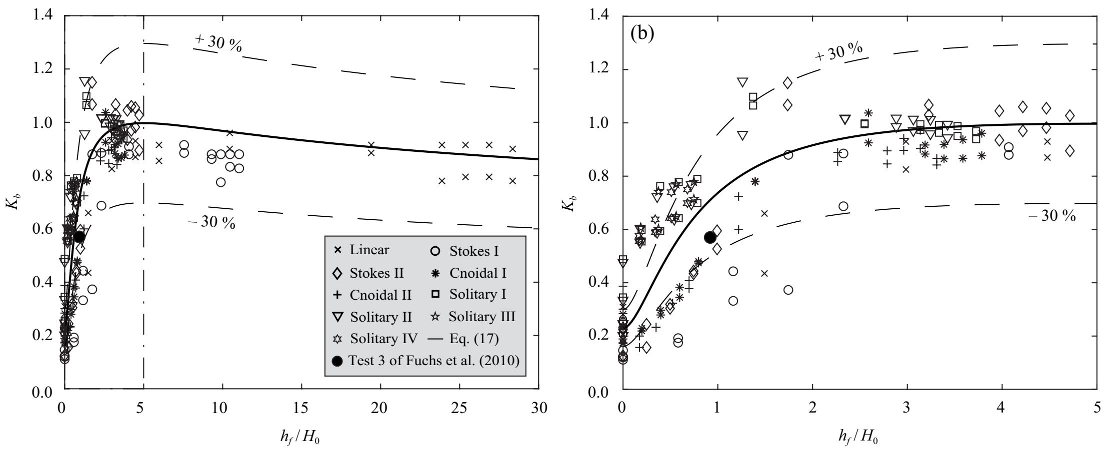

Figure 13: Transformation coefficient K_b for all investigated wave types and bathymetries versus h_f/H_0; (——) represents Eq. (17) and (— —) ±30% bounds with (a) for the entire dataset and (b) for a zoom in the range $0 < h_f/H_0 < 5$.

The equivalents to Eqs. (15) to (17) for $K_{a,b}$ are given by

$$K_{a,b} = 0.34 + 0.66\left(\frac{2(h_f/h_0)}{1+(h_f/h_0)^2}\right)^{8/5}; \quad \text{MSE} = 0.025 \tag{18}$$

$$K_{a,b} = 0.34 + 0.66\left(\frac{1.35[(h_f/h_0)(a_0/H_0)]}{0.39+[(h_f/h_0)(a_0/H_0)]^{1.65}}\right)^{2}; \quad \text{MSE} = 0.027 \tag{19}$$

$$K_{a,b} = 0.34 + 0.66\left(\frac{1.29(h_f/H_0)}{0.59+(h_f/H_0)^{1.1}}\right)^{3}; \quad \text{MSE} = 0.031 \tag{20}$$

The fits of Eqs. (18) to (20) to the data are shown in Appendix C.

As Eqs. (15) to (20) reduce to a constant value for $h_f = 0$ (corresponding to the shoreline in the beach bathymetry), the variability of H_b/h_0 is investigated separately for these cases where $H_b = a_b = \eta_{max} - z''_{bed}$ at the shoreline. Fig. 14 shows the data for H_b/h_0 for all beaches. The best data fit is represented by

$$H_b/h_0 = 8(L_f/H_0)^{-1}; \quad \text{MSE} = 0.002 \tag{21}$$

valid in the range $35 \leq \frac{L_f}{H_0} \leq 1050$ and spanning from deep to shallow water. Eq. (21) generally follows the simulation results and slightly underestimates approximate linear waves, i.e. the waves with the smallest H_0 and, in turn, larger L_f/H_0. However, approximate linear waves are unlikely to be generated during a landslide-tsunami event, especially in 2D or a narrow geometry.

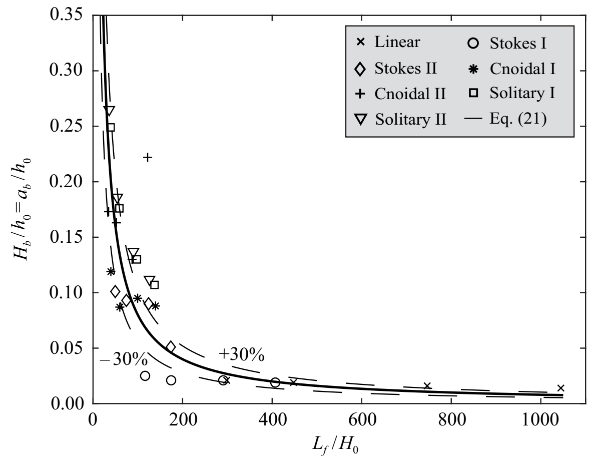

Figure 14: Normalised transformed wave height H_b/h_0 versus the normalised beach length L_f/H_0 for all beach data; (——) represents Eq. (21) and (— —) the ±30% bounds.

6. Discussion

Together with a discussion of the results, this section illustrates the performance of the new empirical equations by taking the variability of the bathymetry into account. In addition, a comparison between 2D and 3D geometries with variable bathymetries is conducted to investigate the combined effect of the bathymetry and water body geometry. Recommendations on the best suited forecast method for each initial condition are also given. Finally, a hazard assessment procedure is illustrated with the 2014 Lake Askja landslide-tsunami.

6.1. Effect of the bathymetry

It has been validated that Green's law, i.e. Eq. (9), can be applied for all the investigated wave conditions during the shoaling process on beach bathymetries. However, only for cnoidal and solitary waves (Table 7) shoaling can be divided into gradual (Eq. (9)) and rapid (Eq. (10)). For solitary waves the transition from the first to the latter occurs for beach slopes $\leq 1/50$ in agreement with Synolakis and Skjelbreia (1993). If a prediction is needed in a section where h decreases over the feature, these equations may be used up to shallow water breaking, e.g. $H/h > 0.78$ (Dean and Dalrymple, 1991), as highlighted in Table 7. In addition, approximate linear, Stokes and cnoidal waves follow the two decay laws in Eqs. (11) and (12) after breaking with small run-ups (Section 3.2). Solitary waves are larger due to the much larger momentum involved and lower energy dissipation.

For bathymetries other than beaches, h_f plays a major role for the initiation of breaking and reflection, heavily affecting H_b/h_0, a_b/h_0 and the upwave conditions. The latter is not directly important for the main propagation direction of tsunamis, but it is an important factor to consider in hazard assessment, especially when h is rapidly decreasing. In general, the effects caused by these phenomena are inversely proportional to h_f/h_0. H_b even reduces to 0.16 of H_0 for cases with $h_f/h_0 = 0.1$ and the reflected H enhances the upwave H by up to a factor of ~ 1.5 (Fig. 9b) for the step bathymetry with $h_f/h_0 = 0.1$. When $h_f/h_0 > 1$, H_b/h_0 is little or not affected compared to values found for a horizontal bathymetry, whereas a_b/h_0 is noticeably affected due to the waves adjusting to the larger water depth and becoming more symmetrical with respect to the mean water level.

Apart from those in Section 6.3, all numerical simulations were carried out in a 2D geometry in this study, hence excluding the effect of the water body geometry. For this reason, in real and wider water body geometries, the effect of the bathymetry is expected to be smaller since the energy spreads on a larger area, as discussed in Section 6.3.

6.2. Regression analysis equation performance

The prediction capabilities of Eqs. (15) to (20) are summarised in Table 5 comparing their MSE values. Note that, even though discrepancies between target and predicted values are not negligible, a wide range of conditions with non-linear effects were investigated. Additionally, it is stressed that the main goal was to develop equations able to capture the general physics of the problem with a good balance between ease of application for hazard assessment and accuracy. In Fig. 15 each equation, represented by different markers, is solved for every investigated initial condition and their predictions are compared with the numerical results.

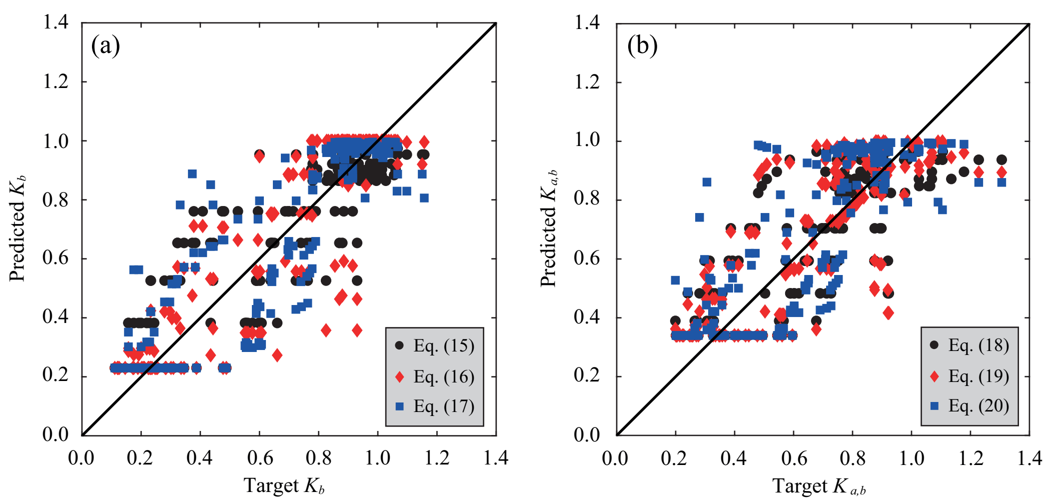

Figure 15: Comparison of target values and prediction for (a) K_b by using Eqs. (15) to (17) and (b) $K_{a,b}$ for Eqs. (18) to (20).

Table 5: Prediction capabilities for the equations derived through regression analysis.

Variable	Equation	MSE
K_b	Eq. (15)	0.021
K_b	Eq. (16)	0.024
K_b	Eq. (17)	0.024
$K_{a,b}$	Eq. (18)	0.025
$K_{a,b}$	Eq. (19)	0.027
$K_{a,b}$	Eq. (20)	0.031

Eqs. (16) and (19) represent the best compromise between accuracy and a detailed description of the initial condition of the incoming tsunamis. These tsunami characteristics are captured by a_0/H_0, which is indicative of the wave types. In addition, they achieved the closest fit to the results from Fuchs et al. (2010) (Section 5). Table 7 summarises the most suitable prediction methods for different conditions.

6.3. The effects of the bathymetry and water body geometry combined

To gain insight into the combined effects of the bathymetry and the water body geometry, additional simulations were conducted in a 3D geometry, by using a rectangular numerical domain of up to 77 m by 45.2 m, using a rectangular grid. These simulations involved approximate linear and solitary I waves spanning from deep- to shallow-water conditions. They were conducted with a uniform h (0.60 m for deep-water and 0.30 m for shallow-water) and for the steepest positive Gaussian bathymetric feature with $h_f/h_0 = 0.1$, with the wave source $b' = 0.6$ m at the radial distance of $r' = 0$ m. Wave gauges were placed at wave propagation angles of $\gamma' = 0°$, 30°, 45° and 60° at intervals of a relative radial distance $\Delta r' = 2.5h_0$.

The results of these tests are shown in Fig. 16 for H, and in Fig. D.1 for a, with a direct comparison between the results with and without the Gaussian bathymetric feature. The waves follow the same decay in both bathymetries up to the location of h_f where shoaling occurs. In Fig. 16 three isolated peaks of different magnitudes and at different relative distances are found for each γ' in both wave types. By using the wavefront length (Ruffini et al., 2019)

$$l_w = b' + 2r'\theta_{rad}, \tag{22}$$

where θ_{rad} is the water body side angle in radians, the decay of the peaks follows approximately Green's law for h = constant. By further considering the variability with γ', the decay follows

$$H_p(r', \gamma', \theta)/h_0 = H_{p,0}/h_0 \left(\frac{l_{w,0}}{l_w(r', \theta)}\right)^{1/2} \cos^2(\gamma'\psi). \tag{23}$$

In Eq. (23), $H_p(r', \gamma', \theta)$ is the wave height of the peak at the position r' and γ' for a defined water body side angle θ, $H_{p,0}$ is the peak at $\gamma' = 0°$, $l_{w,0}$ the corresponding wavefront length and ψ is a wave-type specific multiplication factor. $\psi = 1/3$ for the approximate linear and $\psi = 4/5$ for the solitary I waves. The same relationship applies to a using Eq. (23) by substituting H with a and using $\psi = 1/3$ for the approximate linear and $\psi = 3/5$ for the solitary I waves. These peaks are not present in the results for the 2D geometry (Fig. 8) due to the laterally constraint wave energy.

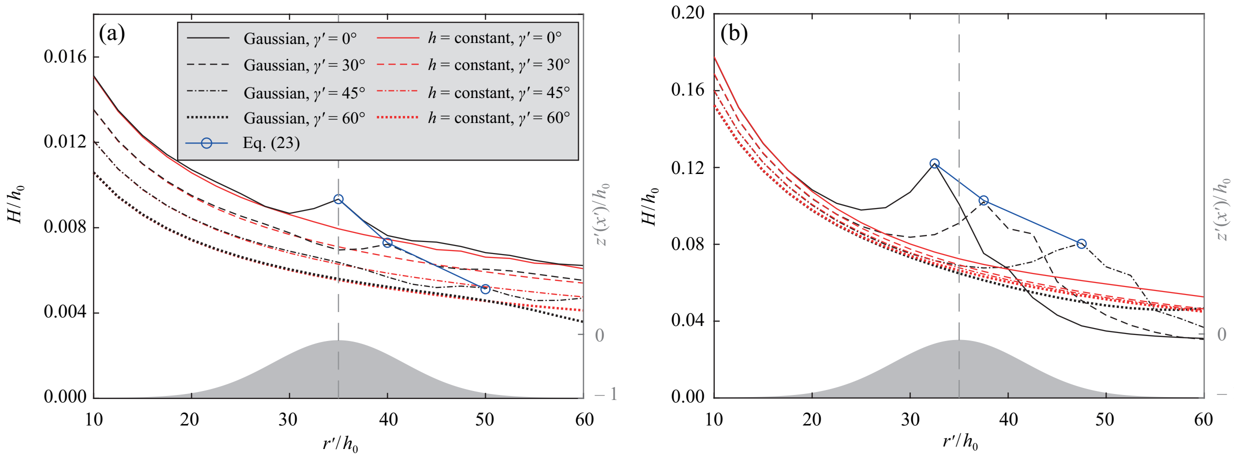

Figure 16: Comparison of the normalised wave height H/h_0 with r'/h_0 and the propagation angle γ' for a 3D geometry with h = constant and the positive Gaussian bathymetric feature with $h_f/h_0 = 0.1$ for (a) approximate linear and (b) solitary I waves. (— —) represent the positions of the crests of the bathymetries and the shaded areas represent the bathymetries.

Table 6: Transformed wave height $\Delta H_b = (H_{b,g}/H_{b,h} - 1) \times 100$ and amplitude $\Delta a_b = (a_{b,g}/a_{b,h} - 1) \times 100$ differences between the Gaussian bathymetric feature with $h_f/h_0 = 0.1$ and the horizontal bathymetry for 2D (subscript 2D) and 3D (subscript 3D) geometries for $\gamma' = 0°$.

Geometry	Wave condition	ΔH_b	Δa_b
2D	approximate linear	−27.9%	−25.7%
2D	solitary I	−43.0%	−42.0%
3D	approximate linear	+2.45%	+2.26%
3D	solitary I	−41.0%	+14.2%
		$\Delta H_{b,\text{3D}} - \Delta H_{b,\text{2D}}$	$\Delta a_{b,\text{3D}} - \Delta a_{b,\text{2D}}$
2D versus 3D	approximate linear	+30.4%	+28%
2D versus 3D	solitary I	+2.0%	+56.2%

The results of H and a for both the 2D and 3D geometries are summarised in Table 6 using $\Delta H_b = (H_{b,g}/H_{b,h} - 1) \times 100$ and $\Delta a_b = (a_{b,g}/a_{b,h} - 1) \times 100$ between the Gaussian (subscript g) and the horizontal (subscript h) bathymetries. Note that a comparison can only be drawn between 2D and 3D for $\gamma' = 0°$ at $x' = r' = 60h_0$ (corresponding to $x'' = 50h_0$) as this is the only direction available in 2D. The additional directions $\gamma' > 0°$ are included in 3D only to investigate the lateral energy spread. The results of H at $\gamma' = 0°$ between the two geometries show that, in 2D, $\Delta H_b = -27.9\%$ whereas for the 3D geometry $\Delta H_b = -2.45\%$ (Table 6). Very similar values, as expected for the approximate linear waves with $H \cong 2a$, are also found for a. The behaviour of solitary I waves is more complex since the difference at $\gamma' = 0°$ is very similar for H between the 2D ($\Delta H_b = -43.0\%$) and 3D ($\Delta H_b = -41.1\%$) geometries. In contrast, the a behaviour compared to a 2D geometry changes (Table 6). Note that this difference for a between 2D and 3D is due to the wave not having fully recovered after propagating over the bathymetry for the 3D case.

These results show that the application of Eqs. (15) to (20) gives a better prediction of H in geometries other than 2D for more shallow-water waves, where the effect of the bathymetry is significant, with a decay difference between 2D and 3D of only $\Delta H_{b,\text{3D}} - \Delta H_{b,\text{2D}} = 2.0\%$. However, for deep-water waves the relations derived for a 2D geometry may underestimate the wave characteristics by up to $\Delta H_{b,\text{3D}} - \Delta H_{b,\text{2D}} = 30.4\%$ if used in a 3D geometry (Table 6) where the transformed waves are almost unaffected by the changing bathymetry (Fig. 16a). A summary of the best suited forecast method for each possible initial condition is presented in Table 7.

Table 7: Summary of the best suited forecasting methods for different initial conditions. Equations with * are from Synolakis and Skjelbreia (1993). The wave types can be derived with the wave type product T from Heller and Hager (2011).

	Stokes waves	Cnoidal waves	Solitary waves
Shoaling on beaches in laterally constrained geometries (2D)	Eq. (9)* to predict H (for a replace H with a and a_0 with H_0 in Eq. (9)).	Eq. (9)* for $h_0/L_f \geq 1/20$ Eqs. (9)* and (10)* for $h_0/L_f < 1/20$ to predict H (for a replace H with a and a_0 with H_0 in Eqs. (9) and (10)).	Eq. (9)* for $h_0/L_f \geq 1/30$ Eqs. (9)* and (10)* for $h_0/L_f < 1/30$ to predict H (for a replace H with a and a_0 with H_0 in Eqs. (9) and (10)).
Effect of the bathymetry in laterally constrained geometries (2D)	Eqs. (16) and (19) or ANN to predict K_b and $K_{a,b}$.	Eqs. (16) and (19) or ANN to predict K_b and $K_{a,b}$.	Eqs. (16) and (19) or ANN to predict K_b and $K_{a,b}$.
Effect of the geometry and bathymetry in laterally unconstrained geometries (3D)	Semi-empirical equations Eqs. (E.2) and (E.3) to predict H_b and a_b.	Semi-empirical equations Eqs. (E.2) and (E.3) to predict H and a at the start of the bathymetric feature, then Eqs. (16) and (19) or ANN to predict K_b and $K_{a,b}$.	Semi-empirical equations Eqs. (E.2) and (E.3) to predict H and a at the start of the bathymetric feature, then Eqs. (16) and (19) or ANN to predict K_b and $K_{a,b}$.

6.4. Real case application

The 2014 Lake Askja landslide-tsunami is used to validate the ANN and Eqs. (16) and (19). All predictions are compared to the numerical results of Gylfadóttir et al. (2017). Gauge 22 (g22) of Gylfadóttir et al. (2017) in Fig. 17 is used for this purpose. This gauge is positioned immediately downwave a steep decrease in h, i.e. the contour lines are close to each other (Fig. 17). Shoreward the bathymetry flattens with a much smaller inclination up to the shoreline.

Appendix E describes a complete procedure to estimate the wave characteristics when both the effects of the bathymetry and water body geometry are significant. This includes the steps from Ruffini et al. (2019) and additional steps, marked with *, which are only relevant for changing bathymetries (Table 7). Step 1: The dimensional parameters are defined, as summarised in Table 8, where the landslide width b, thickness s, mass m_s, density ρ_s, impact velocity V_s, slope angle α, water density ρ_w and water depth h are shown. In Table 9 the landslide non-dimensional parameters are summarised including the slide relative thickness S, the slide relative mass M, the slide Froude number F, the wave type product T and the impulse product parameter P. Step 2: T reveals that the landslide-tsunami is a cnoidal wave. Step 3: The initial tsunami characteristics are calculated (taken from Ruffini et al. (2019) for this case) for a 2D geometry based on Heller and Hager (2010) including the maximum wave height H_M and amplitude a_M as well as the coupling distance d_M between generation and propagation zones (Table 9).

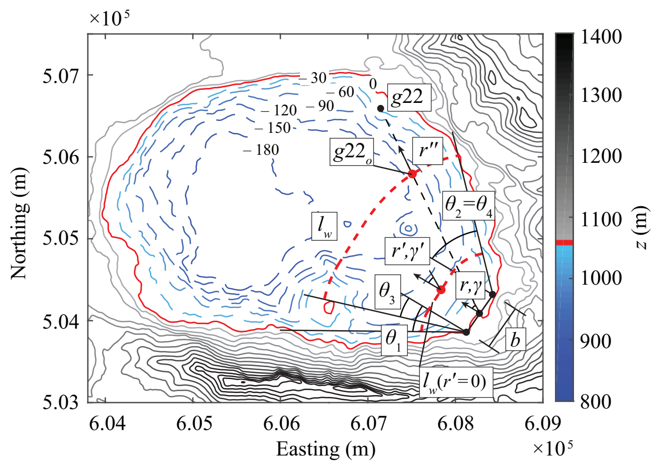

Figure 17: Computation example for g22 of Gylfadóttir et al. (2017). The red line indicates the SWL = 1058 m above sea level. The contours represent a spacing of $\Delta z = 30$ m in global coordinates with dashed lines and solid lines representing the terrain elevation below and above the SWL, respectively.

Table 8: Dimensional landslide parameters for the 2014 Lake Askja case.

b (m)	s (m)	m_s (kg)	ρ_s (kg/m^3)	α (°)	V_s (m/s)	ρ_w (kg/m^3)	h (m)
550.0	35.5	2×10^{10}	2000	10.4	30.1	1000	138.0

Step 4: The initial water body side angles $\theta_1 = 32.4°$ and $\theta_2 = 44.1°$ are evaluated at the slide impact sides (Fig. 17) and used to calculate the wavefront length $l_w(r = d_M, \theta) = 550 + 32.4(\pi/180)531 + 44.1(\pi/180)531 = 1259$ m at the interface between generation and propagation zones where r is the radial distance from the slide impact. As the geometry already starts to diverge at $r = 0$ rather than at $r' = 0$, r' is replaced with r in Eq. (22) (Ruffini et al., 2019). Step 5: Energy conservation is applied for the 2D values H_M and a_M (Table 9) to consider the reduction of the wave magnitude due to the wider geometry compared to 2D resulting in $H(r' = 0, \gamma' = 0°, \theta) = H_M(r' = 0, \gamma' = 0°, \theta = 0°)[b/l_w(r' = 0, \theta)]^{1/2} = 43.3[550/1259]^{1/2} = 28.6$ m and $a(r' = 0, \gamma' = 0°, \theta) = 22.9$ m (Eq. (E.1)).

Table 9: Non-dimensional landslide parameters for the 2014 Lake Askja case.

S	M	F	T	P	d_M (m)	H_M (m)	a_M (m)
0.26	1.91	0.82	1.21	0.49	531	43.3	34.7

Step 6*: A line (dashed black line in Fig. 17) joining the centre of the landslide to the gauge position is drawn, indicating the wave propagation direction. The coordinates of the deepest point upwave of the steep bathymetry is used to identify the starting position of the bathymetric feature with $x'' = 0$ and to obtain the initial water depth $h_0 = 143$ m. Step 7: For that specific point, indicated with g22$_o$ (r = 1822 m, γ = 32.0°, see Fig. 17), where γ is the propagation angle from the slide impact, the geometry side angles are calculated as $\theta_3 = 19.2°$ and $\theta_4 = 44.1°$ and the wavefront length $l_w(r = 1822 \text{ m}, \theta) = 550 + 19.2(\pi/180)1822 + 44.1(\pi/180)1822 = 2563$ m. r' is again replaced by r in Eq. (22). Step 8: H_0 and a_0 at g22$_o$ are calculated using Eqs. (E.2) and (E.3) resulting in H_0 = 19.94 m with β = 1.03 and a_0 = 13.18 m with $\beta = 0.85$ (Table E.1). The effect of the water body geometry is taken into account up to this position, which is then used as the new coordinate system origin $x'' = 0$ at the start of the bathymetric feature for Eqs. (16) and (19) as well as the ANN. Step 9*: The water depth h_f = 26 m at g22 (x'' = 939 m) is calculated to define $h_f/h_0 = 0.18$. Step 10*: Eqs. (16) and (19) are applied and the results are multiplied by H_0 and a_0, respectively, to find H_b and a_b. The wave characteristics are summarised in Table 10 and compared with the numerical results of Gylfadóttir et al. (2017) at g22 as discussed below together with the results from the ANN.

Table 10: Predicted wave parameters based on Eqs. (16) and (19) compared to the numerical parameters of Gylfadóttir et al. (2017) at g22. The values $(\Delta f = f_{pred}/f_{num} - 1) \times 100$ are shown in brackets.

	Predicted	Gylfadóttir et al. (2017)
H_b (m)	7.8 (−49.4%)	15.4
a_b (m)	5.8 (−40.2%)	9.7

To apply the ANN, step 9* requires the calculation of $L_f/(h_0 - h_f)$, T and L_0 as additional parameters. First, the length of the feature L_f = 939 m is calculated as the distance between g22$_o$ and g22 and the difference in bed elevation as $h_0 - h_f = 117$ m resulting in $L_f/(h_0 - h_f) = 8.0$. The offshore wave period is calculated using the maximum wave period $T = T_M = 9\text{P}^{1/2}(h/g)^{1/2} = 9 \cdot 0.49^{1/2} \cdot (138/9.81)^{1/2} = 23.6$ s with Eq. (4) from Heller and Hager (2010) and the wavelength is defined as $L_0 = cT = (9.81 \cdot 143)^{1/2} \cdot 23.6 = 884$ m with c as the shallow water wave celerity. Step 10*: The ANN is applied using all the initial parameters defined in Section 2.2. The output of the ANN is $K_b = 0.59$ and $K_{a,b} = 0.74$. These parameters, are used to obtain H_b and a_b, respectively, which are summarised in Table 11.

Table 11: Wave parameters predicted by the ANN compared to the numerical parameters of Gylfadóttir et al. (2017) at g22. The values $(\Delta f = f_{pred}/f_{num} - 1) \times 100$ are shown in brackets.

	Predicted	Gylfadóttir et al. (2017)
H_b (m)	11.8 (−23.4%)	15.4
a_b (m)	9.8 (+1.0%)	9.7

Eqs. (16) and (19) resulted in a deviation of $\Delta f(H_b) = -49.4\%$ and $\Delta f(a_b) = -40.2\%$ (see Table 10), respectively, in predicting the wave characteristics of Gylfadóttir et al. (2017) (Table 10). The ANN results in a better overall performance (Table 11), with $\Delta f(H_b) = -23.4\%$ and $\Delta f(a_b) = +1.0\%$.

The discrepancies found between the present study and Gylfadóttir et al. (2017) may be associated with the non-linear interaction of the effect of the bathymetry and water body geometry. The energy continues to spread laterally downwave of g22$_o$ whilst the wave is propagating over the bathymetric feature hence altering the effect on the waves and changing wave breaking which may occur sooner in the 2D geometry. Based on the investigation of the combined effect of the bathymetry and water body geometry (Section 6.3), the equations derived for a 2D geometry are expected to result in accurate predictions for H_b even in wider geometries for solitary waves. In fact, the same decays of approximately 40% were found in both 2D and 3D at $\gamma' = 0°$ (Table 6). However, for less non-linear waves the decay predicted by these equations and the ANN may be too large. This is due to the bathymetry affecting H_b and a_b very little, resulting in values close to the ones with a horizontal bathymetry. The landslide-tsunami classified as cnoidal wave (step 2) in the Lake Askja case is expected to be under-predicted by methods derived from 2D geometries due to the non-linearity being rather low for this wave type ($H_0/h_0 = 0.14$). This explains the lower values from the presented study compared to the values of Gylfadóttir et al. (2017) (Tables 10 and 11). However, a degree of uncertainty must also be attributed to Gylfadóttir et al. (2017) neglecting the deformation of the landslide, which has an impact, especially during tsunami generation. Further, in the direction of g22 the run-up was slightly overestimated compared to the real event indicating that the offshore waves at g22 were also larger than in reality.

7. Conclusions

This study is aimed at developing reliable prediction methods for landslide-tsunami hazard assessment by taking the effect of the bathymetry on idealised tsunami propagation into account. The non-hydrostatic non-linear shallow water model SWASH was used to conduct simulations, mainly in a 2D geometry (laterally constrained tsunami energy) with a uniform width of 0.60 m. This enabled to separate the effect of the bathymetry from the effect of the water body geometry. Three different bathymetry classes were investigated: linear beach, submerged positive and negative Gaussian bathymetric features and positive and negative steps with the water depth at the crest/trough of the bathymetric feature ranging from $0.1h_0 \leq h_f \leq 1.9h_0$, where h_0 is the initial water depth. Nine different idealised landslide-tsunamis were simulated, ranging from deep- to shallow-water, i.e. one approximate linear, two Stokes, two cnoidal and four solitary waves (Table 2) over all aforementioned bathymetries (apart of two solitary wave conditions for which only selected bathymetries were used) resulting in a total of 184 tests.

The spatial distribution of the wave height H and amplitude a for the beach bathymetry were first validated by using theoretical shoaling formulations for solitary waves (Synolakis and Skjelbreia, 1993). Two prediction methods were used to obtain the transformed idealised landslide-tsunami characteristics downwave of every investigated bathymetry namely an Artificial Neural Network (ANN) and a regression analysis. Both methods were developed to forecast the transformation coefficient $K_b = H_b/H_0$, i.e. the ratio between the transformed wave height H_b downwave of the bathymetric feature and the incident wave height H_0, and the amplitude transformation coefficient $K_{a,b} = a_b/a_0$, i.e. the ratio between transformed a_b and incident wave amplitude a_0 to the initial idealised landslide-tsunami and bathymetry. The first method is capable of linking two sets of data without prior assumptions, which was convenient to investigate the large number of different conditions. However, the regression analysis is based on a physical understanding of the phenomenon and it considers a smaller number of input variables, allowing a simpler computation. This method relied on h_f/h_0, $(h_f/h_0)(a_0/H_0)$ or, alternatively, h_f/H_0 as independent variables. In addition to the numerically simulated waves, the empirical equations were validated with a laboratory landslide-tsunami propagating over a trapezoidal breakwater from Fuchs et al. (2010). Despite of the ANN outperforming the empirical equations, both methods are suitable to be used due to their complementary strengths and weaknesses.

A comparison was also conducted between simulations in 2D and 3D geometries to quantify the effect of the bathymetry and the water body geometry combined. Simulations were carried out with h = constant and with a Gaussian bathymetric feature with $h_f/h_0 = 0.1$ as an extreme case. This showed that in 3D propagation, approximate linear H_b and a_b are much less affected by the bathymetry than by the geometry, as expected. For more non-linear waves, such as solitary waves, the difference between 2D and 3D is small for H_b when the propagation angle is $\gamma' = 0°$. The contribution of the bathymetry to propagation is similar in 2D and 3D for shallow-water waves, for which only $\Delta H_{b,3\mathrm{D}} - \Delta H_{b,2\mathrm{D}} = 2\%$ is expected. On the other hand, for more deep-water waves the contribution of the geometry becomes more relevant in respect to the bathymetry one for 3D propagation. Under these conditions the results are underestimated by up to $\Delta H_{b,3\mathrm{D}} - \Delta H_{b,2\mathrm{D}} = 30.4\%$ using the proposed prediction methods. Note that, with the 3D geometry, the most extreme cases were investigated and this combined effect is less relevant for more laterally constrained water body geometries, as summarised in Table 7.

A step by step calculation procedure was illustrated with the 2014 Lake Askja case and its results were compared with the simulations of Gylfadóttir et al. (2017). Better performance were generally found with the ANN compared to the equations based on the regression analysis (Eqs. (16) and (19)). The agreement of the ANN with the simulated values of Gylfadóttir et al. (2017) with $\Delta f(H_b) = -23.4\%$ against $\Delta f(H_b) = -49.4\%$ when Eq. (16) was used and $\Delta f(a_b) = +1.0\%$ for the ANN against $\Delta f(a_b) = -40.2\%$ by using Eq. (19). These discrepancies are associated with the non-linear interaction of the effect of the bathymetry and geometry combined and also due to the assumptions made by Gylfadóttir et al. (2017).

The methods presented herein are derived from studying idealised landslide-tsunamis in a 2D geometry. When applied to a 3D geometry the predictions are more accurate for more shallow-water waves, while more deep-water waves tend to be under-predicted (Table 7). However, considering the satisfactory agreement for the 2014 Lake Askja event, the relations and the ANN developed in this study are suitable for initial landslide-tsunami hazard assessment and expand the capability of generic hazard assessment methods.

Future work should consider a wider range of bathymetries by adding cases such as trapezoidal breakwaters and obstacles reaching above the SWL (e.g. islands), both in numerical simulations and laboratory experiments. This will allow to further expand the ANN prediction capabilities.

Acknowledgements

The authors would like to thank Prof. Nicholas Dodd for helpful suggestions and Dr. Sigríður Sif Gylfadóttir and her collaborators for providing data for the Lake Askja case. The University of Nottingham HPC cluster Augusta has been accessed to perform the numerical simulations. The developed ANN can be downloaded from www.drvalentinheller.com.

Notation

$A1'$	[-]	= initial activation values array of the first hidden layer of the ANN
$A1$	[-]	= final activation values array of the first layer of the ANN
$A2'$	[-]	= initial activation values array of the second hidden layer of the ANN
$A2$	[-]	= final activation values array of the second layer of the ANN
$A3'$	[-]	= initial activation values array of the output layer of the ANN
$A3$	[-]	= final activation values array of the output of the ANN
a	[L]	= wave amplitude
a_{th}	[L]	= wave trough amplitude
B	[-]	= bias array
b	[L]	= slide width at the slide impact location
b'	[L]	= source width at the coupling location
Cov	[-]	= covariance
C_r	[-]	= Courant number
c	[L/T]	= wave celerity
c_1	[-]	= position of the centre of the Gaussian bathymetric feature

c_2	[-]	= width of the Gaussian bathymetric feature
c_f	[-]	= bottom friction coefficient
d	[L]	= total water depth
d_M	[L]	= coupling distance
E	[ML^2/T^2]	= wave energy
e	[-]	= exponential
F	[-]	= slide Froude number
f_{num}	[-]	= numerical value
f_{pred}	[-]	= predicted value
f_{target}	[-]	= target value
g	[L/T^2]	= gravitational acceleration
H	[L]	= wave height
H_{m0i}	[L]	= incident significant wave height
H_p	[L]	= peak wave height
h	[L]	= water depth
h_f	[L]	= water depth at the bathymetric feature
$K_{a,b}$	[-]	= amplitude transformation coefficient
K_b	[-]	= transformation coefficient
k	[L^{-1}]	= wave number
L	[L]	= wavelength
L_f	[L]	= bathymetric feature length (first half for Gaussian bathymetric feature)
l_w	[L]	= wavefront length
M	[-]	= relative slide mass
m_s	[M]	= slide mass
N	[-]	= number of samples
n	[T/L$^{1/3}$]	= Manning's coefficient
P	[-]	= impulse product parameter
R_c	[L]	= crest freeboard of a structure
r	[L]	= radial distance from the slide impact
r'	[L]	= radial distance from the coupling location
S	[-]	= relative slide thickness
Std	[-]	= standard deviation
s	[L]	= slide thickness
T	[-]	= wave type product
T	[T]	= wave period
t'	[T]	= time from when the wave reaches the coupling location
$\overline{u}$	[L/T]	= depth averaged velocity in $x'-$direction
$\overline{u}_i$	[L/T]	= incident velocity
V_s	[L/T]	= slide impact velocity
$\overline{v}$	[L/T]	= depth-averaged velocity in $y'-$direction
W	[-]	= weight matrix
$\overline{w}$	[L/T]	= depth-averaged velocity in $z'-$direction
X	[-]	= unscaled array of ANN variables
X_{max}	[-]	= array of maximum values of ANN variables during training
X_{min}	[-]	= array of minimum values of ANN variables during training

x'	[L]	= x'-coordinate from the coupling location
x''	[L]	= x''-coordinate from the start of the bathymetric feature
Y	[-]	= scaled array of ANN variables
y'	[L]	= y'-coordinate from the coupling location
z	[L]	= elevation above sea water level
z'	[L]	= z'-coordinate from the coupling location
z''	[L]	= z''-coordinate from the start of the bathymetric feature
z''_{bed}	[L]	= seabed z''-coordinate

Greek symbols

α	[°]	= slide impact angle
β	[-]	= pre-factor in Eqs. (E.2) and (E.3)
γ	[°]	= wave propagation angle from the slide impact
γ'	[°]	= wave propagation angle from the coupling location
Δa	[-]	= wave amplitude ratio
Δf	[L]	= relative difference between numerical and theoretical wave parameter
ΔH	[-]	= wave height ratio
$\Delta r'$	[L]	= r'-direction wave gauge spacing
$\Delta t'$	[T]	= time step
$\Delta x'$	[L]	= x'-direction grid size and horizontal distance
$\Delta x''$	[L]	= x''-direction wave gauge spacing
$\Delta y'$	[L]	= y'-direction grid size
Δz	[L]	= contours spacing in z-direction
η	[L]	= water surface elevation
η_i	[L]	= incident water surface elevation
η_{max}	[L]	= maximum water surface elevation
θ	[°]	= water body side angle
θ_{rad}	[rad]	= water body side angle in radians
π	[-]	= mathematical constant
ρ_s	[M/L^3]	= slide density
ρ_w	[M/L^3]	= water density
$\rho(\text{pred}, \text{target})$	[-]	= Pearson correlation coefficient for the ANN
ψ	[-]	= pre-factor in Eq. (23)

Subscripts

0	= incident value taken at $x'' = 0$ for h = constant
2D	= 2D geometry
3D	= 3D geometry
b	= transformed
g	= Gaussian bathymetric feature
h	= horizontal bathymetry
i	= incident
j	= counter for j-th data sample
M	= maximum

m	= number of inputs for the ANN
n	= number of neurons for the 1st hidden layer
o	= number of outputs for the ANN
p	= number of neurons for the 2nd hidden layer

Abbreviations

ANN	= Artificial Neural Network
MPI	= Message Passing Interface
MSE	= Mean Square Error
NLSWE	= Non-Linear Shallow Water Equation
pred	= Predicted
SWASH	= Simulating WAves till SHore
SWL	= Still Water Level
2D	= Wave flume geometry
3D	= Wave basin geometry

A. Wave amplitude distributions

The wave amplitude of the approximate linear, Stokes I, cnoidal I and solitary I waves are presented for the beach bathymetry in Fig. A.1, the Gaussian bathymetric feature in Fig. A.2 and the step bathymetry in Fig. A.3.

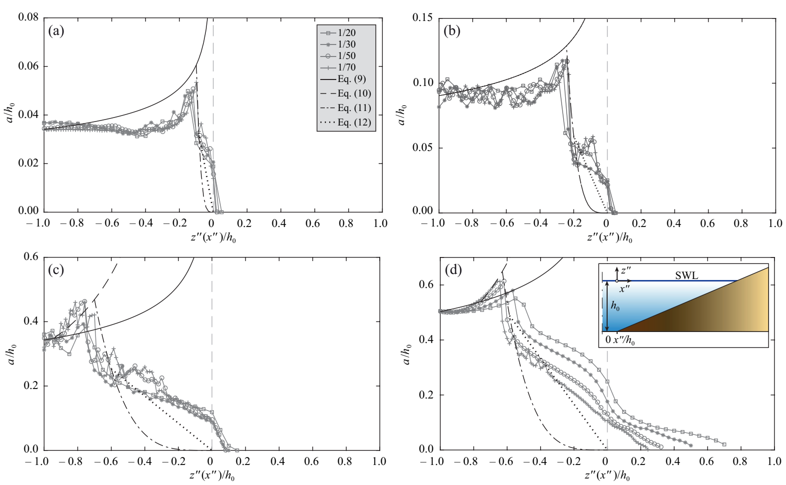

Figure A.1: Linear beach bathymetries: normalised wave amplitudes a/h_0 with $z''(x'')/h_0$ for (a) approximate linear waves, (b) Stokes I waves, (c) cnoidal I waves and (d) solitary I waves compared to Green's law (Eq. (9)), Boussinesq's results (Eq. (10)) and decay laws after breaking (Eqs. (11) and (12)). (— —) represents the position of the shoreline.

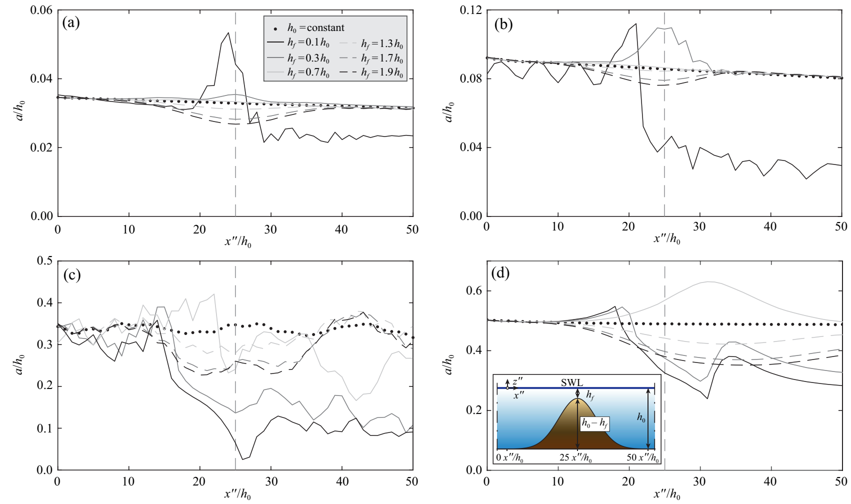

Figure A.2: Positive and negative Gaussian bathymetric features: normalised wave amplitudes a/h_0 with x''/h_0 for (a) approximate linear waves, (b) Stokes I waves, (c) cnoidal I waves and (d) solitary I waves. (— —) highlight x''/h_0 of the maximum or minimum of the bathymetries.

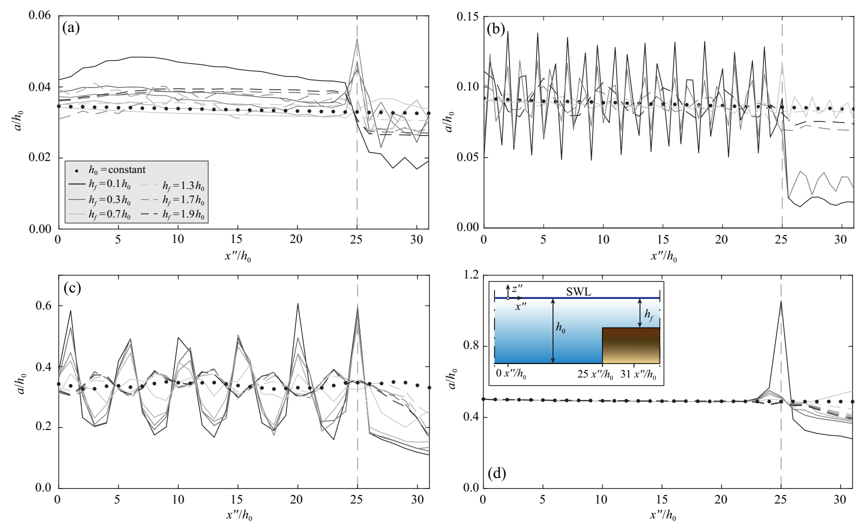

Figure A.3: Positive and Negative step bathymetries: normalised wave amplitudes a/h_0 with x''/h_0 for (a) approximate linear waves, (b) Stokes I waves, (c) cnoidal I waves and (d) solitary I waves. (— —) highlight x''/h_0 the position of the positive or negative step.

B. Details of the ANN

Details of the chosen ANN are presented hereafter with all the required elements to perform a calculation using Section 2.2. First, the inputs are scaled between 1 and −1 with Eq. (5) where the arrays of the maximum and minimum values of all 6 input variables for the training dataset are

$$X_{max} = \begin{bmatrix} 83.330 & 0.589 & 0.589 & 10 & 9.950 & 1.900 \end{bmatrix} \tag{B.1}$$

$$X_{min} = \begin{bmatrix} -83.330 & 0.067 & 0.035 & 2.000 & 3.542 & 0.000 \end{bmatrix}. \tag{B.2}$$

The activation values for each neuron are then calculated by multiplying the results with the weight matrix $W_{\mathrm{n,m}}$ plus the bias array B_{n} (Eq. (6)), which are

$$W_{\mathrm{n,m}} = \begin{bmatrix} -0.5296 & -0.6885 & 1.0928 & 0.9096 & -0.4310 & 0.5370 \\ -0.6613 & 0.3443 & 0.5187 & -0.8013 & -0.5572 & 2.1533 \\ 0.1189 & -0.7561 & 0.3990 & 0.8784 & -0.5174 & -1.9777 \\ -1.3106 & -0.1101 & 1.5049 & 0.9393 & -0.3861 & -0.1054 \\ -1.8950 & -0.8188 & -0.5028 & 0.6529 & 0.2187 & -0.1242 \\ 1.7557 & -0.6158 & -1.2368 & 0.9105 & -0.9121 & 0.3668 \\ 0.3610 & 1.3275 & 1.1716 & 0.6196 & 0.8787 & 1.3374 \\ 0.1056 & -1.2522 & -0.0283 & -0.1833 & -1.2188 & -1.1233 \\ -1.1365 & -0.4485 & 1.2414 & 0.8786 & -0.2110 & -1.3281 \\ 0.4484 & 0.8178 & -0.3037 & 1.1311 & 1.2736 & -0.2911 \\ -0.4787 & 0.9562 & -0.3034 & -1.0019 & 0.3049 & -1.9277 \\ 1.0140 & -0.0724 & 1.1508 & 0.7257 & 0.7134 & -1.7134 \\ 0.8220 & 0.4833 & -1.5005 & 1.1575 & 0.6716 & 0.0861 \\ -0.2139 & -0.9094 & -1.0225 & -0.5123 & 0.8452 & -1.5318 \\ -0.4561 & -0.2400 & 1.3462 & -0.4849 & -0.2768 & 1.3099 \end{bmatrix} \tag{B.3}$$

and

$$B_{\mathrm{n}} = \begin{bmatrix} 2.7287 \\ 1.7854 \\ -1.7649 \\ 1.2000 \\ 1.3712 \\ -1.4016 \\ -0.03271 \\ 0.2827 \\ 0.2374 \\ 1.0561 \\ -1.7002 \\ 0.3765 \\ 1.1736 \\ -1.5095 \\ -2.3011 \end{bmatrix}. \tag{B.4}$$

The activation values are then treated with the Sigmoid symmetric function (Eq. (7)). The process is again replicated for the second layer using the final activation values of the first layer as inputs resulting in

$$
W_{\mathrm{p,n}} = \begin{bmatrix}
0.2268 & -0.1310 & -0.7861 & 0.1316 & 0.5489 & -0.6365 & 0.3425 & -0.7258 & -0.3874 & 0.7038 & 0.1915 & 0.4215 & 0.7714 & 0.3356 & -0.1378 \\
-0.1805 & 0.1130 & 0.7200 & -0.1801 & 0.0666 & -0.7180 & -0.4233 & 0.6953 & 0.5485 & 0.3439 & -0.2944 & 0.0651 & 0.3098 & 0.7259 & -0.0450 \\
-0.6273 & 0.0667 & -0.2704 & -0.2951 & 0.1583 & -0.6730 & 0.6409 & -0.3940 & 0.3278 & 0.7483 & 0.6101 & -0.0627 & -0.4645 & -0.6025 & 0.3731 \\
0.1303 & 0.6473 & 0.3903 & -0.3195 & 0.8378 & 0.2066 & 0.8480 & 0.7556 & 1.0086 & -0.0700 & 0.0077 & 0.5526 & -0.3741 & 0.2922 & ,0.5819 \\
0.6366 & -0.6385 & 0.7042 & 0.6481 & -0.0983 & -0.1254 & -0.7578 & 0.4947 & -0.0233 & 0.7604 & -0.3546 & 0.0861 & 0.1421 & -0.1519 & -0.1820 \\
0.1652 & -0.8132 & 0.4281 & 0.2128 & -0.3817 & -0.5369 & -0.4195 & -0.4154 & -1.5351 & 0.5840 & 1.0828 & 0.6299 & 0.7352 & 0.4969 & 0.1810 \\
-0.5286 & -0.4858 & 0.4847 & -0.6093 & 0.7371 & 0.7080 & 0.2923 & 0.0666 & -0.2705 & -0.4483 & -0.4272 & -0.2809 & -0.5074 & 0.4450 & -0.3428 \\
0.3689 & -0.8664 & 0.8202 & 0.5026 & -0.2494 & -1.5061 & 0.1481 & 0.4592 & -0.1611 & -0.4600 & 1.4622 & 0.7272 & 0.1642 & 0.3598 & -0.4072 \\
-0.1205 & 0.7432 & -0.4721 & 0.7991 & 0.4952 & 0.1513 & -0.0759 & 0.2963 & 0.0319 & -0.3061 & -0.3411 & -0.6221 & -0.5887 & -0.3412 & -0.4556 \\
-0.4773 & -0.0601 & -0.1513 & 0.3728 & -0.5169 & -0.5266 & 0.4379 & 0.5945 & -0.4550 & -0.0690 & 0.1214 & 0.8310 & -0.0323 & -0.4834 & 0.2478 \\
-0.2342 & 0.1132 & 1.1238 & 0.6190 & 0.4702 & 0.3459 & 1.0007 & -0.6063 & -0.2678 & 0.2653 & -0.6188 & 0.4693 & -0.8945 & -0.2583 & 0.4377 \\
-0.1905 & -0.5894 & -0.3068 & 0.2854 & -0.6648 & -0.5091 & 0.5353 & 0.2970 & -0.0285 & -0.2091 & 0.1358 & -0.5184 & -0.3929 & -0.4986 & 0.6665 \\
-0.7685 & -0.0264 & -0.4514 & 0.1834 & 0.2778 & 0.6240 & 0.1419 & 0.3540 & 1.2202 & -0.0317 & 0.3716 & -0.7478 & 0.6393 & -0.4067 & 0.0738 \\
0.2734 & 0.8737 & -0.4520 & -0.0554 & -0.6168 & 0.5912 & 0.0185 & -0.4972 & -0.3619 & 0.4193 & 0.0676 & 0.0881 & -0.1465 & -0.5601 & -0.8105 \\
-0.3018 & 0.1852 & 0.7028 & 0.5548 & 0.2376 & 0.4686 & 0.2803 & 0.2263 & 0.3155 & 0.3848 & 0.5126 & -0.5190 & -0.1318 & 0.7397 & 0.1800
\end{bmatrix} \tag{B.5}
$$

and

$$B_{\mathrm{p}} = \begin{bmatrix} -1.5673 \\ -1.5310 \\ 1.1176 \\ -1.0194 \\ -0.4078 \\ -0.3398 \\ 0.2032 \\ 0.0117 \\ 0.1145 \\ -0.5637 \\ -0.9280 \\ -0.9596 \\ -0.9244 \\ 1.5774 \\ -1.8244 \end{bmatrix}. \tag{B.6}$$

The scaled output, representing the results of the ANN for the new input, is then calculated using Eq. (6) with the output weight matrix

$$W_{\mathrm{o,p}}^{\intercal} = \begin{bmatrix} 0.7397, 0.5437 \\ 0.0257, -0.4493 \\ -0.2598, 0.3055 \\ 0.4970, 0.9532 \\ 0.6938, 0.4977 \\ -0.6808, -1.0325 \\ 0.3187, 0.3403 \\ -0.8505, -0.7570 \\ -0.2803, -0.9016 \\ 0.0011, -0.3347 \\ -0.3491, -1.0875 \\ 0.8740, 0.6773 \\ -0.3991, -0.8662 \\ 0.3185, -0.9878 \\ -0.8206, -0.0109 \end{bmatrix} \tag{B.7}$$

and the bias array

$$B_{\mathrm{o}} = \begin{bmatrix} -0.7149 \\ 0.1142 \end{bmatrix}. \tag{B.8}$$

$W_{\mathrm{o,p}}$ is presented in the transposed form $W_{\mathrm{o,p}}^{\intercal}$ due to space constrictions. Finally, the output is scaled back using the inverse of Eq. (5) with

$$X_{max} = \begin{bmatrix} 1.157 & 1.306 \end{bmatrix} \tag{B.9}$$

$$X_{min} = \begin{bmatrix} 0.111 & 0.199 \end{bmatrix}. \tag{B.10}$$

C. Regression for $K_{a,b}$

Fig. C.1 shows the regression analysis for a_t/a_0 versus h_f/h_0 (Fig. C.1a) and $(h_f/h_0)(a_0/H_0)$ (Fig. C.1b) with the solid black lines representing Eqs. (18) and (19), respectively. In general, a worse performance than for Eqs. (15) and (16) for K_b can be seen. This is mainly due to the larger data spread for $h_f/h_0 > 1.4$ in Fig. C.1a and for $(h_f/h_0)(a_0/H_0) > 0.8$ in Fig. C.1b. Fig. C.2 shows the variability of $K_{a,b}$ with h_f/H_0 and Eq. (20) represented by a solid black line.

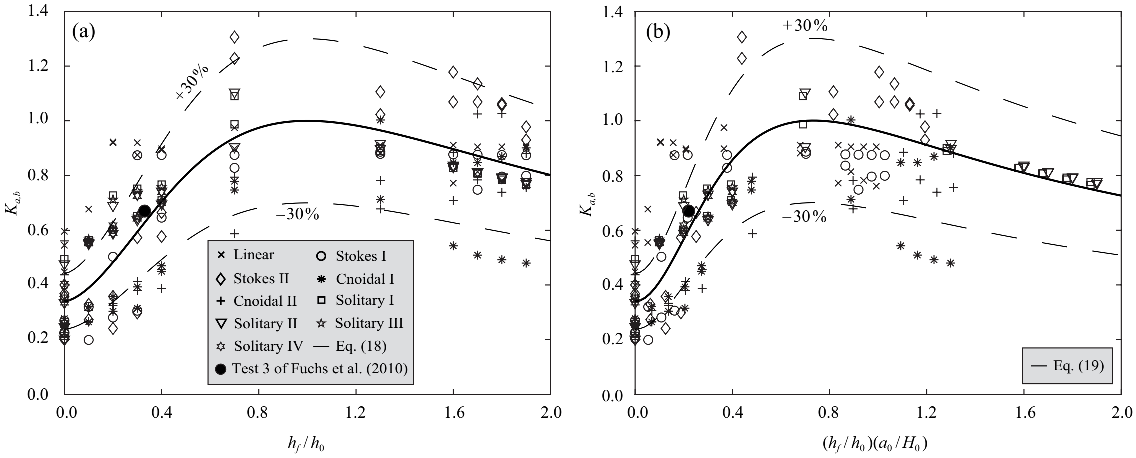

Figure C.1: Transformation coefficient $K_{a,b}$ for all investigated wave types and bathymetries versus (a) h_f/h_0 with (——) Eq. (18) and (b) $(h_f/h_0)(a_0/H_0)$ with (——) Eq. (19); (— —) represent the ±30% bounds.

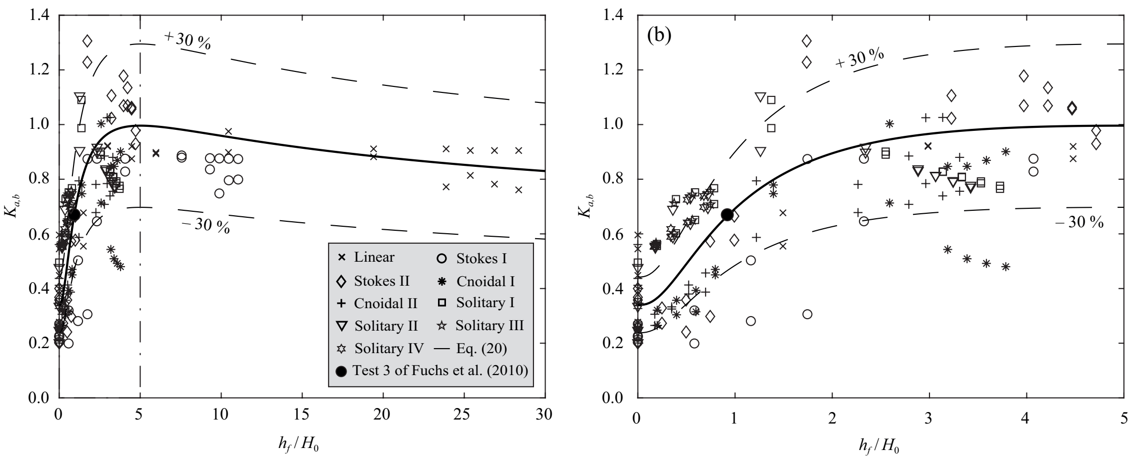

Figure C.2: Transformation coefficient $K_{a,b}$ for all investigated wave types and bathymetries versus h_f/H_0 with (——) Eq. (20) and (— —) the ±30% bounds for (a) the entire dataset and (b) a zoom for the range $0 < h_f/H_0 < 5$.

D. The effect of the bathymetry and water body geometry combined for *a*

Fig. D.1 shows the effect of the bathymetry and water body geometry combined for a in a 3D geometry with $h_f/h_0 = 0.1$ at a Gaussian bathymetric feature. The decay of the maximum peaks can be defined with Eq. (23) with H replaced by a. The same ψ as for H for approximate linear waves is used but a different ψ for solitary I waves (Section 6.3), namely $\psi = 1/3$ for the approximate linear and $\psi = 3/5$ for the solitary I waves.

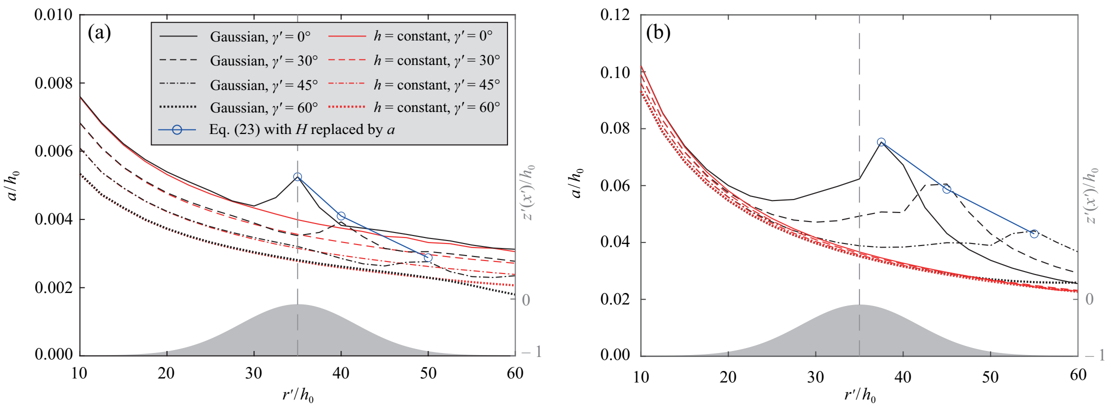

Figure D.1: Comparison of the normalised wave amplitude a/h_0 with r'/h_0 and the propagation angle γ' for a 3D geometry with h = constant and the positive Gaussian bathymetric feature with $h_f/h_0 = 0.1$ for (a) approximate linear waves and (b) solitary I waves. The vertical dashed lines highlight the positions of the crests of the bathymetries.

E. Hazard assessment computation procedure

The procedure to calculate the transformed wave heights considering both the effect of the bathymetry and the water body geometry is summarised here.

1. Define the landslide width b, thickness s, mass m_s, density ρ_s, impact velocity V_s, slope angle α, water density ρ_w and water depth h. Calculate the relative slide thickness S, relative slide mass M, slide Froude number F and the impulse product parameter P.
2. Evaluate the wave type in 2D using the wave type product T based on Heller and Hager (2011).
3. Calculate the maximum wave height H_M for 2D and its position from the slide impact $r = d_M$ (Heller and Hager, 2010).
4. Define θ_1 and θ_2 (Fig. 17) at the slide sides to approximate the current geometry with an idealised one up to $r' = 0$ and calculate the wave front length $l_w(r' = 0, \theta)$.
5. Compute $H(r' = 0, \gamma' = 0°, \theta)$ by applying energy conservation

$$H(r' = 0, \gamma' = 0°, \theta) = H_M(r' = 0, \gamma' = 0°, \theta = 0°)[b/l_w(r' = 0, \theta)]^{1/2}. \tag{E.1}$$

6*. Project a line from the slide centre to the point of interest, identify the start (i.e. the deepest point) $x'' = 0$ of any bathymetric feature along that line and identify h_0.

7. Define θ_3 and θ_4 at the slide sides to approximate the geometry up to an identified point to consider the expansion of the water body and calculate $l_w(r', \theta)$ with r' being its position in the propagation zone. If the bathymetry is significantly changing then use the origin of the bathymetric feature defined in step 6.

8. Calculate the incident wave height H_0 or wave amplitude a_0 using

$$\frac{H_0(r', \gamma', \theta)}{h} / \left(\frac{b'}{l_w(r', \theta)} \right)^{1/2} = \beta \frac{H(r' = 0, \gamma' = 0°, \theta = 0°)}{h} \cos^2 \left(\frac{\gamma'}{3} \right) \tag{E.2}$$

or

$$\frac{a_0(r', \gamma', \theta)}{h} / \left(\frac{b'}{l_w(r', \theta)} \right)^{1/2} = \beta \frac{a(r' = 0, \gamma' = 0°, \theta = 0°)}{h} \cos^2 \left(\frac{\gamma'}{3} \right) \tag{E.3}$$

from Ruffini et al. (2019), where β is a wave type specific pre-factor (Table E.1).

Table E.1: Pre-factors β for H (Eq. (E.2)) and a (Eq. (E.3)) for each investigated wave type (Ruffini et al., 2019).

	H	a
Wave theory	β	β
5^{th} order Stokes	1.10	1.01
5^{th} order cnoidal	1.03	0.85
1^{st} order solitary	1.20	0.84

9*. Calculate h_f of the bathymetric feature for the desired position with $x'' > 0$. If the ANN is used, additional parameters are needed namely the length of the feature L_f between $x'' = 0$ and the desired position at $x'' > 0$, the incident wave period T (using Eq. (4) from Heller and Hager, 2010) and the wavelength calculated with the shallow-water wave theory $L_0 = cT$.

10*. Apply Eqs. (16) and (19), or the ANN, to find the transformation coefficient K_b or the amplitude transformation coefficient $K_{a,b}$ and solve them for H_b and a_b, respectively.

References

References

Baldock, T., Shabani, B., Callaghan, D., 2019. Open access Bayesian Belief Networks for estimating the hydrodynamics and shoreline response behind fringing reefs subject to climate changes and reef degradation. *Environmental Modelling & Software* 119, 327–340.

Beji, S., Battjes, J., 1993. Experimental investigation of wave propagation over a bar. *Coastal Engineering* 19(1), 151–162.

Bellotti, G., Briganti, R., Beltrami, G., 2012. The combined role of bay and shelf modes in tsunami amplification along the coast. *Journal of Geophysical Research: Oceans* 117(8), 1–13.

Blayo, E., Debreu, L., 2005. Revisiting open boundary conditions from the point of view of characteristic variables. *Ocean Modelling* 9(3), 231–252.

Boussinesq, J., 1872. Théorie des ondes et des remous qui se propagent le long d'un canal rectangulaire horizontal, en communiquant an liquide contenu dans ce canal de vitesses sensiblement pareilles de la surface anfond, liouvilles. *Journal de Mathématiques Pures et Appliquées* 17, 55–108.

Chen, F., Heller, V., Briganti, R., 2020. Numerical modelling of tsunamis generated by iceberg calving validated with large-scale laboratory experiments. *Advances in Water Resources* 142, 103647.

Couston, L.A., Mei, C., Alam, M.R., 2015. Landslide tsunamis in lakes. *Journal of Fluid Mechanics* 772, 784–804.

d'Angremond, K., Van Der Meer, J.W., De Jong, R.J., 1997. Wave transmission at low-crested structures, *in: Coastal Engineering 1996*, 2418–2427.

Dean, R.G., Dalrymple, R.A., 1991. Water wave mechanics for engineers and scientists. Volume 2. World Scientific, Singapore.

Dingemans, M.W., 1997. Water wave propagation over uneven bottoms: Part 1. World Scientific, Singapore.

Evers, F., Heller, V., Fuchs, H., Hager, W., Boes, R., 2019a. Landslide generated impulse waves in reservoirs - Basics and computation. 2^{nd} edition. ETH Zurich, Zurich.

Evers, F.M., Hager, W.H., Boes, R.M., 2019b. Spatial impulse wave generation and propagation. *Journal of Waterway, Port, Coastal, and Ocean Engineering* 145(3), 04019011.

Fenton, J.D., 1985. A fifth-order Stokes theory for steady waves. *Journal of Waterway, Port, Coastal, and Ocean Engineering* 111(2), 216–234.

Fenton, J.D., 1999. The cnoidal theory of water waves, *in: Developments in Offshore Engineering*. Elsevier, pp. 55–100.

Fuchs, H., Heller, V., Hager, W.H., 2010. Impulse wave run-over: Experimental benchmark study for numerical modelling. *Experiments in Fluids* 49(5), 985–1004.

van Gent, M.R., van den Boogaard, H.F., Pozueta, B., Medina, J.R., 2007. Neural network modelling of wave overtopping at coastal structures. *Coastal Engineering* 54(8), 586–593.

Green, G., 1838. On the motion of waves in a variable canal of small depth and width. *Transactions of the Cambridge Philosophical Society* 6, 456–462.

Gylfadóttir, S.S., Kim, J., Helgason, J.K., Brynjólfsson, S., Höskuldsson, Á., Jóhannesson, T., Harbitz, C.B., Løvholt, F., 2017. The 2014 Lake Askja rockslide induced tsunami: Optimization of numerical tsunami model using observed data. *Journal of Geophysical Research: Oceans* 122(5), 4110–4122.

Hagan, M., Menhaj, M., 1994. Training feedforward networks with the Marquardt algorithm. *IEEE Transactions on Neural Networks* 5(6), 989–993.

Harbitz, C.B., Glimsdal, S., Løvholt, F., Kveldsvik, V., Pedersen, G.K., Jensen, A., 2014. Rockslide tsunamis in complex fjords: From an unstable rock slope at Åkerneset to tsunami risk in western Norway. *Coastal Engineering* 88, 101–122.

Heller, V., Hager, W.H., 2010. Impulse product parameter in landslide generated impulse waves. *Journal of Waterway, Port, Coastal, and Ocean Engineering* 136(3), 145–155.

Heller, V., Hager, W.H., 2011. Wave types of landslide generated impulse waves. *Ocean Engineering* 38(4), 630–640.

Heller, V., Spinneken, J., 2013. Improved landslide-tsunami prediction: Effects of block model parameters and slide model. *Journal of Geophysical Research: Oceans* 118(3), 1489–1507.

Heller, V., Spinneken, J., 2015. On the effect of the water body geometry on landslide-tsunamis: Physical insight from laboratory tests and 2D to 3D wave parameter transformation. *Coastal Engineering* 104, 113–134.

Huber, A., Hager, W.H., 1997. Forecasting impulse waves in reservoirs. *Transactions of the International Congress on Large Dams* 1, 993–1006.

Jiang, L., LeBlond, P.H., 1994. Three-dimensional modeling of tsunami generation due to a submarine mudslide. *Journal of Physical Oceanography* 24(3), 559–572.

Knowles, J., Yeh, H., 2018. On shoaling of solitary waves. *Journal of Fluid Mechanics* 848, 1073–1097.

Kranzer, H.C., Keller, J.B., 1959. Water waves produced by explosions. *Journal of Applied Physics* 30(3), 398–407.

Lalli, F., Postacchini, M., Brocchini, M., 2019. Long waves approaching the coast: Green's law generalization. *Journal of Ocean Engineering and Marine Energy* 5, 1–18.

Lara, J.L., Losada, I.J., Maza, M., Guanche, R., 2011. Breaking solitary wave evolution over a porous underwater step. *Coastal Engineering* 58(9), 837–850.

Marquardt, D.W., 1963. An algorithm for least-squares estimation of nonlinear parameters. *Journal of the Society for Industrial and Applied Mathematics* 11(2), 431–441.

van der Meer, J.W., Briganti, R., Zanuttigh, B., Wang, B., 2005. Wave transmission and reflection at low-crested structures: Design formulae, oblique wave attack and spectral change. *Coastal Engineering* 52(10), 915–929.

Meng, Z., Hu, Y., Ancey, C., 2020. Using a data driven approach to predict waves generated by gravity driven mass flows. *Water* 12(2), 600.

Öner, M., Deveci Kocakoç, İ., 2017. JMASM 49: A compilation of some popular goodness of fit tests for normal distribution: Their algorithms and MATLAB codes (MATLAB). *Journal of Modern Applied Statistical Methods* 16(2), 30.

Panizzo, A., Briganti, R., 2007. Analysis of wave transmission behind low-crested breakwaters using neural networks. *Coastal Engineering* 54(9), 643–656.

Panizzo, A., De Girolamo, P., Petaccia, A., 2005. Forecasting impulse waves generated by subaerial landslides. *Journal of Geophysical Research: Oceans* 110(C12), 1–23.

Pourzangbar, A., Losada, M.A., Saber, A., Ahari, L.R., Larroudé, P., Vaezi, M., Brocchini, M., 2017. Prediction of non-breaking wave induced scour depth at the trunk section of breakwaters using genetic programming and artificial neural networks. *Coastal Engineering* 121, 107–118.

Pringle, W.J., Yoneyama, N., Mori, N., 2016. Two-way coupled long wave - RANS model: Solitary wave transformation and breaking on a plane beach. *Coastal Engineering* 114, 99–118.

Romano, A., Bellotti, G., Di Risio, M., 2013. Wavenumber-frequency analysis of the landslide-generated tsunamis at a conical island. *Coastal Engineering* 81, 32–43.

Ruffini, G., Heller, V., Briganti, R., 2019. Numerical modelling of landslide-tsunami propagation in a wide range of idealised water body geometries. *Coastal Engineering* 153, 103518.

Stelling, G., Duinmeijer, S.P.A., 2003. A staggered conservative scheme for every Froude number in rapidly varied shallow water flows. *International Journal for Numerical Methods in Fluids* 43(12), 1329–1354.

Stelling, G., Zijlema, M., 2003. An accurate and efficient finite-difference algorithm for non-hydrostatic free-surface flow with application to wave propagation. *International Journal for Numerical Methods in Fluids* 43(1), 1–23.

Strusinska-Correia, A., Oumeraci, H., 2012. Nonlinear behaviour of tsunami-like solitary wave over submerged impermeable structures of finite width. *Coastal engineering proceedings* 1(33), 1–14.

SWASH, T., 2016. SWASH - User manual Version 4.01. Delft University of Technology, Environmental Fluid Mechanics Section.

Synolakis, C.E., Bardet, J.P., Borrero, J.C., Davies, H.L., Okal, E.A., Silver, E.A., Sweet, S., Tappin, D.R., 2002. The slump origin of the 1998 Papua New Guinea tsunami 458(2020), 763–789.

Synolakis, C.E., Skjelbreia, J.E., 1993. Evolution of maximum amplitude of solitary waves on plane beaches. *Journal of Waterway, Port, Coastal, and Ocean Engineering* 119(3), 323–342.

Watt, S.F.L., Talling, P.J., Vardy, M.E., Heller, V., Hühnerbach, V., Urlaub, M., Sarkar, S., Masson, D.G., Henstock, T.J., Minshull, T.A., Paulatto, M., Le Friant, A., Lebas, E., Berndt, C., Crutchley, G.J., Karstens, J., Stinton, A.J., Maeno, F., 2012. Combinations of volcanic-flank and seafloor-sediment failure offshore Montserrat, and their implications for tsunami generation. *Earth and Planetary Science Letters* 319, 228–240.

Watts, P., Grilli, S.T., Tappin, D.R., Fryer, G.J., 2005. Tsunami generation by submarine mass failure. II: Predictive equations and case studies. *Journal of Waterway, Port, Coastal, and Ocean Engineering* 131(6), 298–310.

Wiegel, R.L., Noda, E.K., Kuba, E.M., Gee, D.M., Tornberg, G.F., 1970. Water waves generated by landslides in reservoirs. *Journal of the Waterways, Harbors and Coastal Engineering Division* 96(2), 307–333.

Winckler, P., Liu, P.L.F., 2015. Long waves in a straight channel with non-uniform cross-section. *Journal of Fluid Mechanics* 770, 156–188.

Zijlema, M., Stelling, G., 2005. Further experiences with computing non-hydrostatic free-surface flows involving water waves. *International Journal for Numerical Methods in Fluids* 48(2), 169–197.

Zijlema, M., Stelling, G., Smit, P., 2011. SWASH: An operational public domain code for simulating wave fields and rapidly varied flows in coastal waters. *Coastal Engineering* 58(10), 992–1012.